ISBN 978-91-7501-810-2

Magnetic Fields and Induced Power in the Induction Heating of Aluminium Billets

MARK WILLIAM KENNEDY

KTH Industrial Engineering and Management

Licentiate Thesis in
Materials Science and Engineering
Stockholm, Sweden 2013

www.kth.se

ROYAL INSTITUTE
OF TECHNOLOGY

Magnetic Fields and Induced Power in the Induction Heating of Aluminium Billets

Mark William Kennedy

Supervisors: Ragnhild E. Aune and Jon Arne Bakken

Licentiate Thesis

School of Industrial Engineering and Management
Department of Materials Science and Engineering
Royal Institute of Technology
SE-100 44 Stockholm
Sweden

Stockholm 2013

"The reasonable man adapts himself to the world; the unreasonable one persists in trying to adapt the world to himself.

Therefore all progress depends on the unreasonable man."

-George Bernard Shaw (1856 - 1950),
Man and Superman (1903) "Maxims for Revolutionists"

ABSTRACT

Induction heating is a common industrial process used for the reheating of billets before extrusion or forging. In this work the influence of the coil and work piece geometry, the effect of the electrical properties of the work piece, and the coil current and frequency, on the magnetic flux density and resulting work piece heating rates were studied. A combination of 1D analytical solutions, 2D axial symmetric finite element modelling and precise measurements has been used.

Dozens of heating and magnetic field experiments have been conducted, with steadily increasing sophistication and measurement accuracy. The development of the experimental techniques will be described in the 'cover' and related to the later results published in the supplements. Experimental results are compared to predictions obtained from analytical and numerical models. The published measurements obtained for the billet heating experiments consisted of: billet electrical conductivity with <0.5% error, applied currents with <1% error, magnetic flux densities with 1-2% error, calorifically determined heating rates with <2% error and electrical reactive power with <~2% error. 2 D axial symmetric finite element models were obtained, which describe the measured results with less than a 2% difference (i.e. an 'error' of the same magnitude as the measurement uncertainty). Heating and reactive power results predicted by the FEM model are in excellent agreement with analytical solutions from 50 Hz to 500 kHz (differences from <1% to 6%).

A modified 1D short coil correction factor is presented which accounts for the interaction of the coil and work piece geometry, electrical properties and operating frequency, on the average magnetic flux density of the coil/work piece air-gap and the resulting heating rate. Using this factor, the average magnetic flux density in the air-gap can be estimated analytically within 2-3% and the heating rates of billets of known electrical properties can be estimated, with typical errors on the order of 5%.

Keywords: Induction, heating, billets, coils, magnetic fields.

ACKNOWLEDGMENTS

I would like to thank my primary supervisor, Prof. Ragnhild E. Aune for the opportunity to return to university to renew my education and increase my technical skills after many years in industry. The opportunity to study such interesting phenomena in great detail is appreciated.

I am deeply grateful for the electrical and mathematical guidance provided by my secondary supervisor, Prof. E.M. Jon Arne Bakken and by Dr. David Knight. Without their inductance and induction heating tutorials, this work could not have been conducted. I am also thankful for the inductance software provided by Robert S. Weaver and for the proof reading of the various manuscripts contained in this thesis by Dr. Allan MacRae, of MacRae Tech. Inc.

I wish to express gratitude to Egil Torsetnes at NTNU for helping with the design and construction of the experimental apparatus. Sincere gratitude is also due to Kurt Sandaunet at SINTEF for his support and help, as well as for the use of the SINTEF laboratory.

I am indebted to a number of Master's students who have assisted me at various times: Georg Pohle, Robert Fritzsch, and Behzad Mirzaei.

I would also like to thank my wife Elisabeth Stokker for accepting the disruption to our lives, taking care of our 3 children and allowing me the opportunity to apply myself to this academic task.

The present study was carried out as part of the RIRA (Remelting and Inclusion Refining of Aluminium) project funded by the Norwegian Research Council (NRC) - BIP Project No. 179947/I40. The industrial partners involved in the project are: Hydro Aluminium AS, SAPA Heat Transfer AB, Alcoa Norway ANS, Norwegian University of Science and Technology (NTNU) and SINTEF Materials and Chemistry. The funding granted by the industrial partners and the NRC is gratefully acknowledged.

Mark William Kennedy
Stockholm, May 2013

SUPPLEMENTS

The present thesis includes the following supplements:

Supplement 1: "Improved Short Coil Correction Factor for Induction Heating of Billets," M.W. Kennedy, S. Akhtar, J.A. Bakken, and R.E. Aune, Presented at the 3rd International Symposium on High Temperature Metallurgical Processing, Orlando Florida, March 11-15, 2012.

3rd International Symposium on High-Temperature Metallurgical Processing, Edited by: Tao Jiang, Jiann-Yang Hwang, Patrick Masset, Onuralp Yucel, Rafael Padilla, and Guifeng Zhou, TMS, ISBN 978-1-11829-141-2, 2012, 373-382.

Supplement 2: "Analytical and FEM Modeling of Aluminum Billet Induction Heating with Experimental Verification," M.W. Kennedy, S. Akhtar, J.A. Bakken, and R.E. Aune, Presented at Light Metals 2012, Orlando Florida, March 11-15, 2012.

Light Metals 2012, Edited by: Carlos E. Suarez TMS, ISBN 978-1-11829-139-9, 2012, 269-275.

Supplement 3: "Empirical Verification of a Short Coil Correction Factor," M.W. Kennedy, S. Akhtar, J.A. Bakken, and R.E. Aune, Submitted to the *IEEE Transactions on Industrial Electronics*, November, 2012, Resubmitted March 25, 2013, and to be resubmitted June, 2013.

CONTENTS

Chapter 1

INTRODUCTION

Induction heating has been studied academically and experimentally since before the discovery of the electron. Heaviside published one of the first mathematical treatments of induction heating, studying the heat developed in a 'core' within a solenoidal coil in 1884 [1]. S.Z. De Ferranti patented perhaps the first application of induction to furnace design, in British Patent Specification No. 700, in 1887 [2, 3]. The practical development of various channel furnaces for steel making quickly followed through the late 19th and early 20th centuries [4-6]. The development of 'high frequency' coreless induction furnaces from about 1918-1930 by E.F. Northrup, represents a key advance pertinent to this thesis [7-11].

It was understood by early workers in the field of coreless induction heating, that coils and work pieces of typical dimensions, e.g. with a diameter of approximately the same magnitude as their height, did not produce the same magnetic field strength as a 'long' coil, nor did this field interact 'perfectly' with the work piece. Northrup demonstrated his depth of knowledge in his patent filed in 1924 [11], via the proposed use of a 'coupling' factor, to describe the variation of the coil magnetic flux, with the coil and work piece dimensions. Burch and Davis proposed the use of the Nagaoka coefficient [12] in their book from 1928 [13] to correct for the impact of coil and work piece shortness. A similar method using the Nagaoka coefficient was proposed by Stansel in 1944 [14]. Vaughan and Williamson proposed the use of an empirically modified Nagaoka short coil correction factor in their paper of 1945 [15]. This factor was subsequently 'squared' and republished without reference by Tudbury as his "Workpiece Shortness Correction Factor" in 1960 [16]. Baker proposed an alternate methodology for the correction of the magnetic field strength for coil shortness in his paper of 1957 [17], without any detailed explanation of the derivation. Lavers proposed perhaps the most advanced analytical method in 1970 [18], which appears to have been immediately superseded by the adoption of modern computerized numerical methods.

1.1 Project Objectives

In the present work, 'coreless' coils have been applied to the heating of non-ferromagnetic billets with the purpose of studying the interaction of the magnetic field produced by the coil with the work piece, and the impact of the work piece on the magnetic flux density in the coil/work piece air-gap.

The main objectives of this work were to determine:

1. The correct method of calculating the magnetic flux density of an empty air-core coil of finite size.
2. The affect of work pieces of various dimensions on the magnetic flux density in the air-gap of different coils.
3. A method of correlating the relationship between the dimensions of the coils and work pieces, with the magnetic flux density in the air gap.
4. The accuracy of the new correlation by direct measurement of work piece heating rates, and by the application of 2D axial symmetric finite element modelling, to determine the impact of operating frequency.

Thus, the present work is intended to trace the following flow diagram.

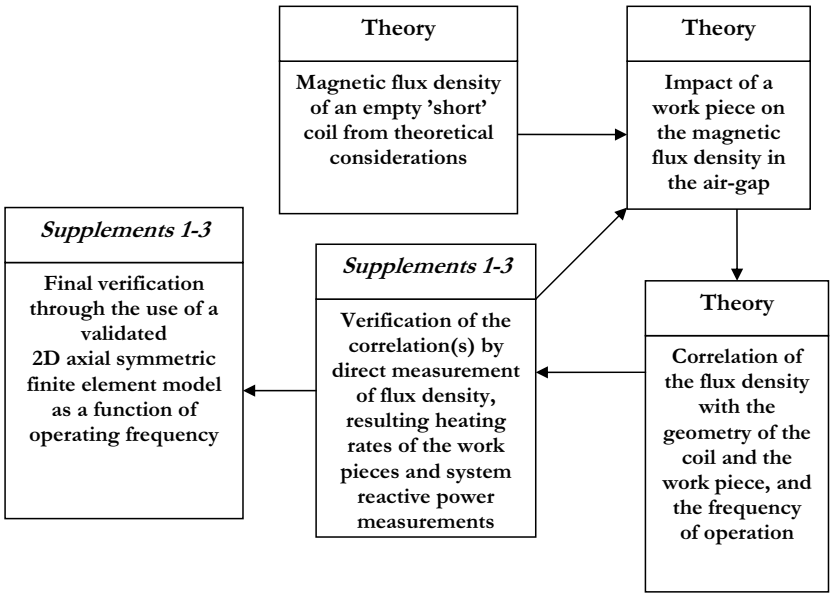

Figure 1.1-Schematic outline of the thesis and *Supplements*.

This thesis will examine the required electromagnetic theory in detail, in order to provide the reader with sufficient background to appreciate the following supplements:

In *Supplement 1* the most detailed description of the final water-cooled billet heating experiments are presented, along with most of the experimental heating data. The use of water-cooling allowed experiments to be executed at a thermal steady state and to obtain direct measurement of the heating rate induced in the billets by calorific means. Water-cooling also maintained the outer surface of the work pieces at a sufficiently low temperature, to permit safe measurement of the magnetic flux densities using Hall Effect probes, the results of which are presented in *Supplements 2* and *3*. Experimental heating results are compared with the analytical solutions produced using a frequency corrected version of Vaughan and Williamson's original short coil correction factor [15] and against 2D axial symmetric modelling results at frequencies from 50 Hz to 500 kHz.

In *Supplement 2* the 2 D axial symmetric finite element model is described in some detail. The analytical and numerical methods used to determine the required size of the 'magnetic domain' and the mesh spacing are presented. The exact means of determining and correcting the work piece resistivity and conductivity for use with the analytical and FEM models are described, including a new equation useful to estimate the temperature coefficient of resistivity of aluminium. Analytical magnetic flux density predictions are compared with FEM predictions and measurements for an air-core coil. Experimental results of the impact of a work piece on the magnetic flux density of a 'short' coil are presented and compared with the 2D axial symmetric model results, as a means of benchmarking the model's accuracy. FEM calculated heating rate results are compared with experimental results and analytical predictions at 50 Hz to 500 kHz.

The main results of the thesis are summarized in *Supplement 3*, providing additional data not previously shown in *Supplements 1* and *2*. Heating data from 4 coils, 3 work pieces, high and low current and high and low cooling water flow are presented. A total of 11 conditions with repeats (22 tests) are summarized. Calorific heating and electrical reactive power measurements are compared with the analytical and FEM model solutions, showing excellent agreement. Magnetic flux data from the 'short' induction coil are presented and compared with theoretical predictions and FEM model results with and without a work piece. A highly compact dimensionless formula for the solution to the Biot-Savart law is presented, as a function of coil diameter to length ratio (shape factor) and dimensionless coil length. The final frequency corrected short coil correction factor is presented with the theoretical basis. The limitations and bias caused by the correction factor's semi-empirical nature are discussed in some detail, based on both the experimental heating, reactive power and magnetic flux density measurements.

Chapter 2

THEORY

2.1 Magnetic Flux Density and Inductance of 'Long' and 'Short' Coils

The magnetic field of a very 'long' coil can be easily found by the application of Ampère's [19] or the Biot-Savart law [20]. Using Ampère's original law and ignoring the displacement current:

$$\oint_C \vec{B} \bullet \delta\vec{l} = \mu_0 \mu_r \iint_s \vec{J} \bullet \delta\vec{s} = \mu_0 \mu_r I_{enclosed} \qquad (1)$$

Where $\vec{B}$ [T] is the magnetic flux density parallel to the an infinitesimal vector length $\delta\vec{l}$ and tangent to the closed curve *C*, μ_0 is the permeability of free space (4π x10^{-7} [H/m]), μ_r is the relative magnetic permeability (with recommended values of 1.0000 for air, copper and aluminium [unitless]), $\vec{J}$ [A/m^2] is the current density normal to closed curve *C*, $\delta\vec{s}$ [m^2] is an infinitesimal vector area of surface S normal to $\vec{J}$ and $I_{enclosed}$ [A] is the total enclosed current or $\vec{J} \cdot S$. The orientation of $\vec{B}$ relative to $\vec{J}$ is given by the right hand rule, and both are vector quantities. When written as *B* and *J* in this text, Root Mean Square (RMS) magnitudes are implied.

Equation (1) is applied to a very 'long', i.e. infinite solenoidal coil, a finite length of which is pictured in Figure 2.1. The total current enclosed by the closed path, whose sides are length l_c is clearly $N_c \cdot I_c$. Current is passing out of the page at the top and into the page at the bottom. The flux density within the coil is B_∞, which has a direction from left to right in accordance with the right hand rule. As the coil extends from and to infinity, the flux lines are parallel to l_c, having only a z-component. Thus it can be immediately concluded that there is no magnetic flux external to the coil and $B \cdot l_c = 0$.

On both of the sides of the box, the magnetic flux is perpendicular to the length and thus there is no parallel component and $\vec{B} \bullet \delta\vec{l} = 0$. Integrating around the closed path it is

then immediately seen that Equation (1) yields $B_\infty \cdot l_c = \mu_0 \mu_r N_c \cdot I_c$. Solving for B_∞ results in Equation (2).

$$B_\infty = \frac{\mu_0 \mu_r N_c \cdot I_c}{l_c} \tag{2}$$

where B_∞ is the flux density of a length l_c of a very 'long' or infinite coil, N_c is the number of turns of the coil and I_c is the current per turn [A RMS].

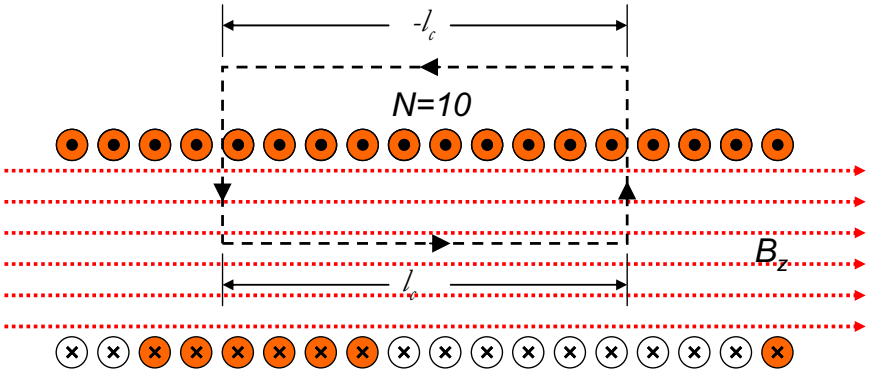

Figure 2.1-Magnetic field produced by 10 turns of an infinite solenoid, indicating a magnetic field present only on the interior of the coil and in the z-direction.

Equation (2) is however, not valid for a coil with length less than 'infinity'. In a short coil the flux is not homogenously distributed as shown in Figure 2.1 and is not parallel with the coil axis, having both a z-component and an r-component. The flux density exterior to a 'short' coil is non-zero, hence the external magnetic reluctance may become a significant factor in determining the total coil magnetic flux density.

The inductance of a 'real', i.e. non-infinite coil, is determined by the number of flux linkages per unit current or:

$$L_c = \frac{A_c N_c B_z}{I_c} \tag{3}$$

where L_c is the inductance of the coil [H], A_c is the area of the coil [m^2], and B_z is now the z-component of the magnetic flux density [T]. B_z being the z-component of the magnetic flux density, clearly links all the coil turns N. The radial component B_r will be

symmetrical around the central axis, and integrating in polar coordinates will result in zero net contribution.

An idealized solenoidal coil, known as a 'current sheet' inductor is shown in Figure 2.2.

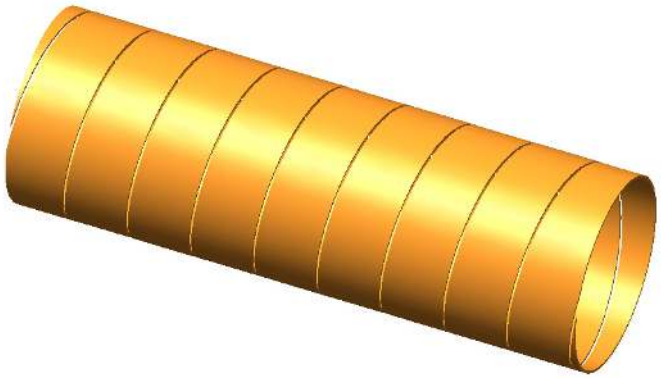

Figure 2.2-10 turn helical 'current sheet' coil or solenoid [21].

A current sheet has a number of properties:

1. The current is purely a surface current, as the sheet is 'infinitely' thin.
2. The coil conductor has no internal volume and hence no internal inductance.
3. The cuts between the turns are infinitesimally thin and hence the entire length is available for conduction.
4. As the cuts between the turns are so thin, there is no leakage flux and all of the z-component of the magnetic flux produced by the coil, links with all of the turns.

B_z can be found using Equation (3) if the inductance is known. In 1879 Lorenz [22] published a formula to solve for the inductance of a current sheet inductor, such as the one shown in Figure 2.2. His formula involved the use of difficult to solve complete elliptical integrals. Lorenz's original formula reformulated into SI units [23], is shown in Equation (4).

$$L_c = \frac{8\mu_0\mu_r N_c^{\,2} r_{cs}^{\,3}}{3l_c^{\,2}}\left[\frac{2k^2-1}{k^3}E(k)+\frac{1-k^2}{k^3}K(k)-1\right] \qquad (4)$$

where r_{cs} is the radius of the current sheet [m], k is the modulus and $K(k)$ and $E(k)$ are the complete elliptical integrals of the first and second kinds.

Modulus *(k)* is defined by Equation (5):

$$k = \sqrt{\frac{4r_{cs}^{\,2}}{4r_{cs}^{\,2} + l_c^{\,2}}} \tag{5}$$

In 1909 Nagaoka [12] reformulated Lorenz's formula using the shape factor (D_{cs}/l_c), where D_{cs} is defined as the current sheet diameter [m]. In Nagaoka's formulation the inductance of a short coil can be found by a combination of Equations (3-5) using a simple 'short coil correction factor', which will be referred to in this text as k_N, in honour of Nagaoka.

$$L_c = k_N \frac{\mu_0 \mu_r N_c \cdot I_c}{l_c} \cdot \frac{A_c N_c}{I_c} = \frac{k_N \mu_0 \mu_r N_c^{\,2} A_c}{l_c} = \frac{k_N \mu_0 \mu_r N_c^{\,2} \pi r_{cs}^{\,2}}{l_c} \tag{6}$$

where k_N, the Nagaoka coefficient is defined by Equation (7) [23]:

$$k_N = \frac{4}{3\pi}\left[\frac{\sqrt{1+u^2}}{u^2}\left(K(k) - E(k)\right) + \sqrt{1+u^2}\,E(k) - u\right] \tag{7}$$

and where u is defined as equal to the shape factor (D_{cs}/l_c).

Nagaoka solved Equation (7) for discrete values of the shape factor (D_{cs}/l_c) to 6 decimal places in his original manuscript [12]. Weaver has now written software to numerically solve the same equation to double precision [24], and this software was used in the preparation of this thesis [25].

From Equation (6) it is obvious that B_z from equation (3) is equal to $k_N \cdot B_\infty$ or:

$$B_z = \frac{k_N \mu_0 \mu_r N_c \cdot I_c}{l_c} \tag{8}$$

In 1928 Wheeler published an empirical formula for the inductance of real short coils with finite wire thickness and coil length [26], as shown in Equation (9) in both the original form and with SI units.

$$L_{\mu H} = \frac{r_i^{\,2} N_c^{\,2}}{9r_i + 10l_i} = \frac{r_{cs}^{\,2} N_c^{\,2}}{0.2286 r_{cs} + 0.254 l_c} \tag{9}$$

where $L_{\mu H}$ is the inductance of the real short coil [μH], r_i is the coil radius measured on the wire centre-line [inches], and l_i is the coil length measured end-to-end [inches].

Knight [27] recently reformulated Equation (9) in SI units to directly solve for the Nagaoka coefficient, k_N:

$$k_N = \frac{1}{1 + 0.4502 \left(\frac{D_c + \delta_c}{l_c} \right)} \tag{10}$$

where D_c is defined as the coil inner diameter [m] and δ_c is the electromagnetic penetration depth into the coil [m] given by:

$$\delta_c = \sqrt{\frac{\rho_c}{\pi \mu_o \mu_r f}} \tag{11}$$

where ρ_c is the electrical resistivity of the coil [Ω·m], and f is the frequency [Hz].

The electrical resistivity is the inverse of the electrical conductivity:

$$\rho_c = \frac{1}{\sigma_c} \tag{12}$$

where σ_c is the coil electrical conductivity [S/m]. For 100% International Annealed Copper Standard (IACS) copper, the recommended conductivity is 58.0 MS/m [28].

Comparing the results of Equation (10) with those given by Weaver's software [25] for Equation (7), indicates that empirical Equation (10) is accurate to approximately 3 significant figures for coils with shape factors typical of induction coils, i.e. from about 0.5 to 2.0, as indicated in Table 1. The use of Equation (10) rather than Equation (7) does not add any significant error in the calculation of induction furnace coil flux densities, given that state of the art Hall Effect Gauss meters have a typical accuracy on the order of 0.5 to 1% for AC magnetic fields, and the ability to measure the work piece heating rates is typically worse (e.g. ~2% error or larger).

Table 1-Comparison of Nagaoka Short Coil Correction Factors Calculated by Numerical Solution of Equation (7) and Using the Empirical Equation (10) [*Supplement 3*].

Shape Factor (D_{cs}/l_c)	**k_N Equation (7)**	**k_N Equation (10)**	**Difference (%)**
0.048	0.980	0.979	-0.11
0.122	0.950	0.948	-0.23
0.50	0.818	0.816	-0.23
0.75	0.748	0.748	-0.02
1.00	0.688	0.690	0.17
1.25	0.638	0.640	0.28
1.50	0.595	0.597	0.31

For a coil with a shape factor of 1, very typical of induction coils, Equation (7) indicates that the coil will have only 69% of the z-component magnetic flux density of the equivalent 'long coil'. To have 95% of the long coil magnetic flux density, the coil would need to have a shape factor of 0.122, and to have 98%, it would need to have a shape factor of 0.048. It is therefore concluded that all typical induction coils are 'short' and that Equation (2) can not be accurately applied to any standard induction problem, i.e. Equation (2) will always result in an empirically measureable error.

For coils constructed of round wire, it has been found that $(D_c + \delta_c)/l_c$ can be equated to the average coil diameter measured from the centre-to-centre of the conductors of the coil, in accordance with classical inductance calculations, i.e. the equivalent 'current sheet' diameter (D_{cs}) should be used, as it will minimize the errors (in the heating estimates) taken over a large range of frequencies (e.g. 50 Hz to 500 kHz). The equivalent current sheet is the dimension where ½ of the current is inside and ½ outside of the chosen diameter. D_{cs} is then located on the coil tubing centreline for both the DC and infinite frequency (surface current) limits. Rosa's round wire correction has not been applied [29], as the present work was performed using coils constructed from hollow tubing and the correction has been found to be excessive [*Supplement 3*].

It is clear from Equations (8) and (10) that the magnetic flux density varies strongly with shape factor. It is relatively easy to solve the Biot-Savart law [20], Equation (13), along the centre-line of a solenoidal coil.

$$\delta\vec{B} = \frac{\mu_o I_c}{4\pi}\frac{\delta\vec{l}\times\hat{r}}{r^2} \tag{13}$$

where $\delta\vec{B}$ is the incremental flux density [T] measured at a point, which is distance of r [m] away from a current carrying conductor, $\delta\vec{l}$ is an incremental distance along the conductor [m] and $\hat{r}$ is a unit vector pointing from $\delta\vec{l}$ toward the measuring point.

Solving Equation (13) along the centre-line of a 'current sheet' solenoid yields:

$$B_0 = \frac{\mu_0 N_c I_c}{2 l_c}\left(\frac{x l_c}{\sqrt{\left(x l_c\right)^2 + r_{cs}^{\,2}}} + \frac{(1-x) l_c}{\sqrt{\left((1-x) l_c\right)^2 + r_{cs}^{\,2}}} \right) \tag{14}$$

where B_0 is the z-component of the flux density [T] along the central axis of a solenoidal coil of length l_c, [m], with current sheet radius r_{cs} [m] and where x is the dimensionless coil length. For $l_c >> r_{cs}$, Equation (14) simplifies to Equation (2).

Dividing Equation (14) by Equation (2) yields a dimensionless centre-line flux density, which is independent of current and the number of coil turns, and somewhat analogous to the Nagaoka coefficient [*Supplement 3*].

$$\frac{B_0}{B_\infty} = \frac{1}{2}\left(\frac{x l_c}{\sqrt{\left(x l_c\right)^2 + r_{cs}^{\,2}}} + \frac{(1-x) l_c}{\sqrt{\left((1-x) l_c\right)^2 + r_{cs}^{\,2}}} \right) \tag{15}$$

Equation (15) has been plotted as a function of coil shape factor in Figure 2.3. From Fig. 2.3 it can be expected that flux density varies strongly with shape factor and varies along the axial length of a given coil (and also in the radial direction, which is not shown). Very long coils (D_{cs}/l_c <0.3) have relatively homogeneous fields near their centre. It is interesting to note that very short coils (D_{cs}/l_c>3) also have relatively homogenous fields along their centre-lines, while longer coils (D_{cs}/l_c <0.6) have steep gradients near the ends of the coils.

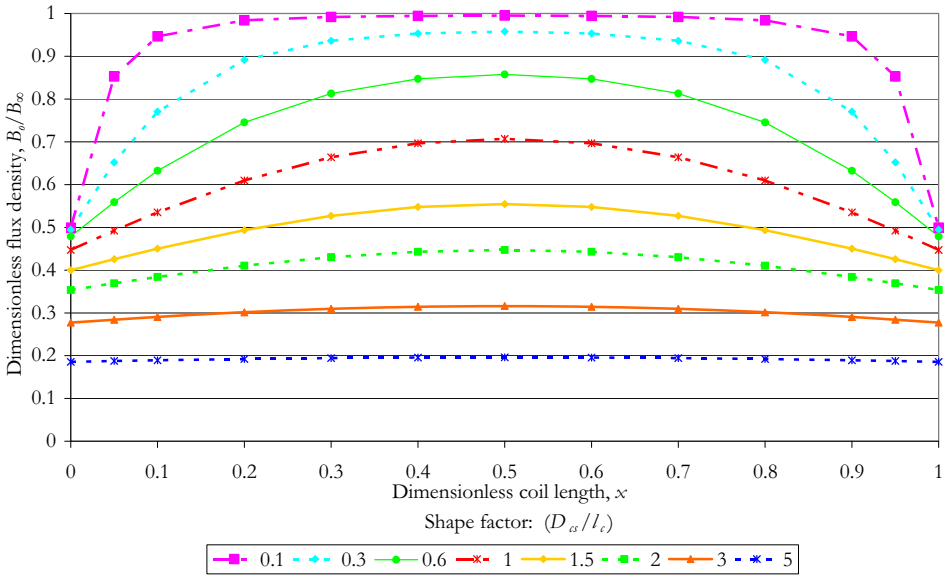

Figure 2.3-Dimensionless coil centre-line flux density (B_0/B_∞) as a function of coil shape factor (D_{cs}/l_c) and dimensionless coil length (x) [30].

2.2 Electromagnetic Induction

Electromagnetic induction can be understood beginning with Ampère's [19] and Faraday's laws [31]. The mathematics are simplified by ignoring the displacement current $\left(\frac{\partial \vec{D}}{\partial t}\right)$ and assuming the system to be at rest:

$$\nabla \times \vec{H} = \vec{J} \tag{16}$$

where $\vec{H}$ is the magnetic field intensity [A (-turns)/m], and $\vec{J}$ is the current density [A/m^2].

In short coils $\vec{H}$ has both a z-component and an r-component. Only the z-component is considered in this analysis, which produces current in the phi direction according to Equation (16).

$$\nabla \times \vec{E} = -\frac{\partial \vec{B}}{\partial t} \tag{17}$$

where $\vec{E}$ is the electric field [V/m], and $\frac{\partial \vec{B}}{\partial t}$ is the change in the magnetic flux density per unit time [T/s].

The relationship between $\vec{B}$ and $\vec{H}$ is given by:

$$\vec{B} = \mu_0 \mu_r \vec{H} \tag{18}$$

From Equation (1) or by applying Stokes's theorem to Equation (16) we can then see that:

$$\oint_C \vec{H} \bullet \delta \vec{l} = I_{enclosed} \tag{19}$$

Similarly applying Stokes' theorem to equation (17) yields the integral form of Faraday's law:

$$\oint_C \vec{E} \bullet \delta \vec{l} = -\frac{\partial \Phi}{\partial t} \tag{20}$$

where $\frac{\partial \Phi}{\partial t}$ is change in the magnetic flux per unit time [Wb/s].

A cylindrical work piece undergoing induction heating is pictured in Figure 2.4.

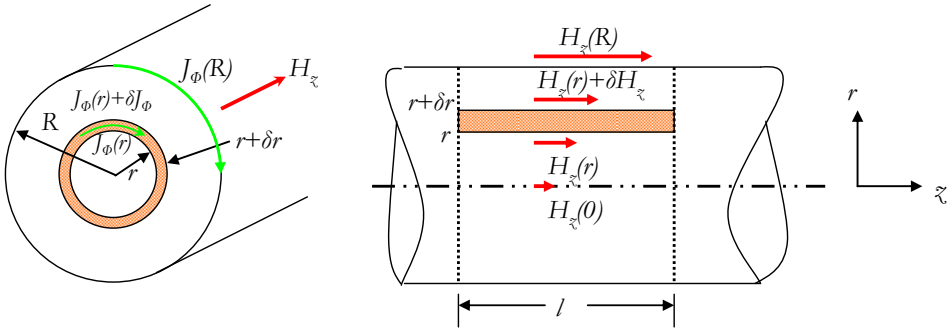

Figure 2.4-Cylindrical work piece undergoing induction heating, please note that *J* and *H* are both complex (time varying) quantities (phasors), with a phase shift and magnitude changing with the penetration depth, only the z-component of the magnetic field intensity and the phi-component of current are considered [32].

Integrating Equation (19) around the box shown in Figure 2.4 [32], and understanding that H_z and J_ϕ are functions of radial position:

$$-H_z l + \left(H_z + \delta H_z\right) l = J_\Phi \delta r \; l \tag{21}$$

And therefore the current density in the phi direction at depth r, J_Φ [A/m^2], is given by

$$J_\Phi = -\frac{\partial H_z}{\partial r} \tag{22}$$

which is also in accordance with the definition of the curl and Equation (16).

In the absence of motion (i.e. neglecting the induced electric field $\vec{v} \times \vec{B}$), Equation (20) can be integrated around the circle shown in Figure 2.4 [32]. The integral must equal zero (no net voltage around a complete circular path) [33] and it is assumed that the work piece is homogeneous and can be represented by a single resistivity ρ_w [Ω·m] and constant relative permeability μ_r.

$$-2\pi r \rho_w J_\Phi + 2\pi\left(r + \delta r\right)\rho_w\left(J_\Phi + \delta J_\Phi\right) + \mu_0 \mu_r 2\pi r \frac{\partial H_z}{\partial t}\partial r = 0 \tag{23}$$

Equation (23) simplifies to (eliminating the term $2\pi\rho_w \delta r \delta J_\Phi$ as negligibly small):

$$\frac{\partial J_\Phi}{\partial r} + \frac{J_\Phi}{r} + \frac{\mu_0 \mu_r}{\rho_w}\frac{\partial H_z}{\partial t} = 0 \tag{24}$$

Combining Equations (22) and (24), yields:

$$\frac{\partial^2 H_z}{\partial r^2} + \frac{1}{r}\frac{\partial H_z}{\partial r} - \frac{\mu_0 \mu_r}{\rho_w}\frac{\partial H_z}{\partial t} = 0 \tag{25}$$

The time-varying vector component $H_z(r,t)$ in Equation (25) can be written: $H_z(r,t) = \sqrt{2}\hat{H}_z(r)\cos[\omega t + \varphi(r)]$, where $\hat{H}_z(r)$ is the RMS magnitude of the magnetic field

intensity and $\varphi(r)$ is the radius dependent phase angle (or phase shift) referenced to the surface of the work piece. $H_z(r,t)$ in Equation (25) can now be replaced by the complex function $\sqrt{2}\underline{H}_z(r)e^{j\omega t}$, where the phasor $\underline{H}_z(r)=\hat{H}_z(r)e^{j\varphi(r)}$ is visualized as a rotating 'mathematical vector' in the complex real-imaginary plane (the under-stroke indicates a complex quantity) [34]. Note that at the surface of the work piece at radius=R, $\varphi(\mathrm{R})=0$ and therefore $\underline{H}_z(\mathrm{R})=\hat{H}_z(\mathrm{R})$. Inserting $\sqrt{2}\underline{H}_z(r)e^{j\omega t}$ in the partial differential Equation (25), it simplifies to the ordinary differential Equation (26):

$$\frac{\partial^2 \underline{H}_z}{\partial r^2}+\frac{1}{r}\frac{\partial \underline{H}_z}{\partial r}-\frac{j\omega\mu_0\mu_r}{\rho_w}\underline{H}_z=0 \tag{26}$$

where j is the $\sqrt{-1}$ and ω is the radial frequency [radians/s].

Equation (26) is a modified Bessel equation of order zero, where the solution is known to be of the form [35]:

$$\underline{H}_z(r)=AI_0\left(\sqrt{j}\left(\frac{\omega\mu_0\mu_r}{\rho_w}\right)^{\frac{1}{2}}r\right)+BK_0\left(\sqrt{j}\left(\frac{\omega\mu_0\mu_r}{\rho_w}\right)^{\frac{1}{2}}r\right) \tag{27}$$

where A and B are integration constants and I_0 and K_0 are the two linearly independent solutions to Equation (26) and are referred to as modified zero order Kelvin Bessel functions of the first and second kind.

Defining the important variable ξ_r, i.e. the dimensionless penetration depth at radius r:

$$\xi_r=\sqrt{2}r\left(\frac{\omega\mu_0\mu_r}{2\rho_w}\right)^{\frac{1}{2}}=\frac{\sqrt{2}r}{\delta_w} \tag{28}$$

where δ_w is the work piece electromagnetic penetration depth, which can found using the work piece electrical resistivity in Equation (11).

Substituting ξ_r into Equation (27):

$$\underline{H}_z(r)=AI_0\left(\sqrt{j}\xi_r\right)+BK_0\left(\sqrt{j}\xi_r\right) \tag{29}$$

The magnetic flux density at $r = 0$ must be finite and since K_0 at $r = 0$ is infinite [33], this solution can be excluded and B must therefore equal zero.

Equation (29) with $B = 0$, can thus be simplified {noting that $I_0\left(\sqrt{j}\,x\right) = J_0\left(j^{3/2}x\right)$}:

$$\underline{H}_z(r) = AI_0\left(\sqrt{j}\xi_r\right) = AJ_0\left(j^{3/2}\xi_r\right) \tag{30}$$

The solution to $J_0\left(j^{3/2}\xi_r\right)$ is in the form $ber\,\xi_r + j\,bei\,\xi_r$ [33], where *ber* and *bei* are the real and imaginary parts of the function J_0.

At the surface of the work piece (radius=R), the magnetic field intensity $\underline{H}_z(R)$, is simply 'the surface magnetic field intensity', H_z which can be evaluated using Equations (8) and (18):

$$H_z = \frac{k^*_N N_c \cdot I_c}{l_c} \tag{31}$$

where k_N^* is a modified Nagaoka, 'short-coil' correction factor accounting for: the geometry of the coil and of the work piece, the electrical properties of the coil and work piece, and the frequency of the applied current, and will be discussed in detail in the next section.

Equation (31) assumes that the magnetic field intensity at the surface of the work piece is equal to the average value in the air-gap. This assumption should tend to result in a slight overestimation, due to the radial gradient present in the air-gap of a short coil. The value of A can be found by substituting Equation (31) into Equation (30) and solving at the outer radius R.

$$A = \frac{k^*_N N_c \cdot I_c}{l_c} \frac{1}{ber\xi_R + jbei\xi_R} \tag{32}$$

where ξ_R is the value of Equation (28) at the outside radius R of the work piece: $\xi_R = \frac{\sqrt{2}R}{\delta_w}$, which is an important characteristic parameter or dimensionless reference thickness.

Substituting A into Equation (30) yields the solution for $\underline{H}_z(r)$:

$$\underline{H}_z(r) = \frac{k^*_N N_c \cdot I_c}{l_c} \frac{ber\xi_r + jbei\xi_r}{ber\xi_R + jbei\xi_R} = \frac{ber\xi_r + jbei\xi_r}{ber\xi_R + jbei\xi_R} H_z \tag{33}$$

The current in the phi direction can now be found by applying Equation (22) to Equation (33) [32]:

$$\underline{J}_\Phi(r) = -\frac{\partial}{\partial r}\left(\frac{ber\xi_r + jbei\xi_r}{ber\xi_R + jbei\xi_R}\right) H_z \tag{34}$$

where $\underline{J}_\Phi(r)$ is the complex current at radius *r*.

Performing the differentiation on Equation (34) yields:

$$\underline{J}_\Phi(r) = -\frac{ber'\xi_r + jbei'\xi_r}{ber\xi_R + jbei\xi_R} \frac{\sqrt{2}}{\delta_w} H_z \tag{35}$$

where *ber'* and *bei'* are the derivatives of *ber* and *bei*.

Evaluating Equation (35) at the surface yields (the negative sign indicates that J produces a magnetic field intensity with a direction, that opposes H):

$$\underline{J}_\Phi(R) = -\frac{ber'\xi_R + jbei'\xi_R}{ber\xi_R + jbei\xi_R} \frac{\sqrt{2}}{\delta_w} H_z \tag{36}$$

The surface RMS current is found using the real part of Equation (36):

$$J_\Phi(R) = -\frac{ber'\xi_R ber\xi_R + bei'\xi_R bei\xi_R}{ber^2\xi_R + bei^2\xi_R} \frac{\sqrt{2}}{\delta_w} H_z \tag{37}$$

The current density is 'negative', opposing the magnetic field that induced it, which results in the induced power (both real and reactive) being negative (power is absorbed and not produced by the work pieces). This fact is indicated by the negative sign in the subsequent equations related to power. RMS power is traditionally considered a positive real number, and will be considered as such in the experimental section to follow.

The Poynting vector evaluated at the surface of the work piece is the electromagnetic energy flux transferred to the work piece [W/m^2]:

$$\vec{S} = \vec{E}_s \times \vec{H}_s \tag{38}$$

In the present axial symmetric case only the phi-component of $\vec{E}_s$ and the z-component of $\vec{H}_s$ are considered. The Poynting vector then has only a radial component:

$$S_r = \underline{E}_{\Phi s} \underline{H}_{zs} \tag{39}$$

where $\underline{E}_{\Phi S}$ is the RMS magnitude of the electric field in the phi direction at the surface and $\underline{H}_{zs}$ is the RMS magnitude of the magnetic field intensity in the z-direction at the surface.

$\underline{E}_{\Phi S}$ and $\underline{H}_{zs}$ are complex phasors and have a phase shift between them, which is evaluated at the surface of the work piece. If the phase shift is referenced to the magnetic field intensity at the surface, making its phase shift at the surface equal to zero, then $\underline{H}_{zs} = H_z$ and its value is therefore 'real'.

The real part of S_r is the 'real' or active power density, P_w/A_w, [W/m^2], while the imaginary part of Equation (39) is the 'imaginary' or reactive power density, Q_w/A_w, [VAr/m^2].

The total real power (in RMS units) [W] is then found by multiplying the total area times the energy density:

$$P_w = \pi D_w l \, \mathrm{Re}\left\{ \underline{E}_s H_z \right\} \tag{40}$$

where the phi-subscript has been eliminated as redundant, H_z is given by Equation (31) and l [m] is the reference length, which is either the length of the coil or of the work piece, whichever is shorter.

From Equation (37) the RMS magnitude of the electric field [V/m] at the surface is given by:

$$E_s = \rho_w J_\Phi(\mathrm{R}) = -\rho_w \frac{\sqrt{2}}{\delta_w} H_z \frac{ber'\xi_R ber\xi_R + bei'\xi_R bei\xi_R}{ber^2(\xi_R) + bei^2(\xi_R)} \tag{41}$$

Therefore from Equation (40):

$$P_w = -\pi D_w l \rho_w \frac{1}{\delta_w} H_z^2 \frac{\sqrt{2}\left(ber\xi_R ber'\xi_R + bei\xi_R bei'\xi_R\right)}{ber^2(\xi_R) + bei^2(\xi_R)} \tag{42}$$

and defining:

$$\varphi(\xi_R) = \frac{\sqrt{2}(ber\xi_R ber'\xi_R + bei\xi_R bei'\xi_R)}{ber^2(\xi_R) + bei^2(\xi_R)} \tag{43}$$

where $\varphi(\xi_R)$ represents the cosine of the phase shift between the induced current and the magnetic field intensity at the surface of the work piece.

Simplifying Equation (42), and substituting for H_z:

$$P_w = -\sqrt{2}\pi l \left(\frac{k_N^* I_c N_c}{l_c}\right)^2 \rho_w \xi_R \varphi(\xi_R) \tag{44}$$

where I_c is the RMS coil current [A]. Note: $l = l_w$ or l_c, whichever is shortest.

Similarly the reactive power Q_w [VAr] in the work piece can be solved for by taking:

$$Q_w = \pi D_w l \,\mathrm{Im}\left\{\underline{E}_s H_z\right\} \tag{45}$$

The imaginary power is then given by:

$$Q_w = -\sqrt{2}\pi l \left(\frac{k_N^* I_c N_c}{l_c}\right)^2 \rho_w \xi_R \Psi(\xi_R) \tag{46}$$

and defining:

$$\Psi(\xi_R) = \frac{\sqrt{2}(bei'\xi_R ber\xi_R - bei\xi_R ber'\xi_R)}{ber^2(\xi_R) + bei^2(\xi_R)} \tag{47}$$

where $\Psi(\xi_R)$ represents the sine of the phase shift between the current and the magnetic field intensity at the surface of the work piece.

It is obvious from Equations (44) and (46), that the 'power factor' of the work piece is given by:

$$P.F. = \frac{\varphi(\xi_R)}{\sqrt{\varphi(\xi_R)^2 + \Psi(\xi_R)^2}} \tag{48}$$

The values of Equations (43), (47) and (48) have been plotted in Figure 2.5 as a function of the value of ξ_R. From Figure 2.5 it can be seen that as the work piece gets larger in diameter or the frequency rises, i.e. for higher ξ_R values, the 'power factor' asymptotically approaches cosine (45^0) or $1/\sqrt{2}$. For ξ_R approaching infinity the electromagnetic penetration depth approaches zero, and ultimately the system has only a surface current or behaves like a 'current sheet', where all of the remaining current has the surface phase shift. For $\xi_R > 5$, $D_w\ \varphi(\xi_R) \approx (D_w - \delta_w)$ and $\Psi(\xi_R)$ becomes almost constant and thus it is possible to have simplified forms of Equations (44) and (46) for these 'high frequency' cases [*Supplement 3*]. At high frequency, the heating rate estimated using Equations (44) and (46) will therefore exhibit a frequency dependence of $\sqrt{f}$. Solutions to all the required Kelvin Bessel functions have been found using software available on-line [25].

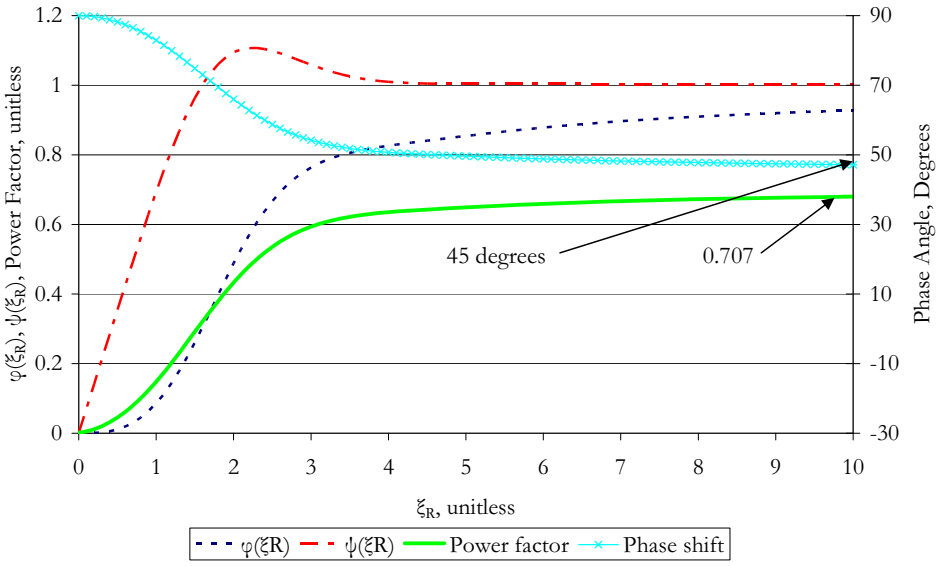

Figure 2.5- Equation (43) [$\varphi(\xi_R)$], Equation (46) [$\Psi(\xi_R)$] and Equation (48) [$P.F. = \cos \Phi$], and phase angle [Φ] as a function of ξ_R.

The *P.F.* plotted in Figure 2.5 is for the work piece only. The overall power factor takes into account the normally considerable reactive power associated with the magnetic flux in the air-gap or insulation between the coil and the work piece ($Q_{air\text{-}gap}$). There is also a reactive power associated with 'real' coils of finite thickness (Q_c) and real power associated with both the work piece and the coil, including leads (P_c). The total system power factor then becomes: $P.F._{total} = \frac{P_w + P_c}{\sqrt{\left(P_w + P_c\right)^2 + \left(Q_w + Q_{air-gap} + Q_c\right)^2}}$, and the overall-phase shift measured across the coil is simply, cos $\Phi_{total} = P.F._{total}$.

It should be noted in applying equation (44):

- heat is assumed to be induced only in the portion of the length shared by both the coil and work piece (any length exceeding the coil length is assumed to have a negligible impact on the system impedance), and
- only the z-component of the magnetic field intensity and phi-component of the current are considered.

Examination of equation (44) reveals that it indirectly contains the square of the average magnetic flux density on the surface of the work piece, i.e. $(k_N^* I_c N_c / l_c)^2$ or $(B_{z\,surface} / \mu_0)^2$. Local work piece heating rates should therefore vary by the square of the local magnetic flux density, which is well known to induction furnace users.

2.3 Impact of the Work Piece on the Magnetic Field Strength of Short Coils

The presence of a work piece inside an 'air-core' coil, alters the magnetic flux density in the coil-work piece 'air-gap' that would be predicted using Equation (8). According to Lenz's law (and the conservation of energy), the current induced in the work piece acts in such a direction as to diminish the magnetic field which produced it. This results in the reduction of magnetic flux and field intensity with depth into the work piece, as described in Section 2.2, by Equation (33).

For large ξ_R values, for example $\xi_R > 5$ [32], the current density and magnetic field intensity gradients in the work piece, can both be adequately described by exponential decay functions of the type:

$$\underline{H}_z(r) \text{ or } \underline{J}_\Phi(r) = C \exp^{-\frac{R-r}{\delta_w}} \tag{49}$$

where C is a value determined by the boundary conditions.

The definition of the electromagnetic penetration depth is actually, "The depth which if occupied by a homogeneous current, would offer the same resistance to the current as the real current distribution in the total conductor." This can be translated as being the depth, which if it were the real conductor depth (i.e. if the conductor where hollow), would offer the same alternating current (A.C.) resistance to the current as the direct current (D.C.) resistance. This definition is only approximately satisfied by the standard definition of the electromagnetic penetration depth, i.e. Equation (11), for 'high frequency' as defined previously (i.e. $\xi_R > 5$).

Equation (49) implies that after 3 electromagnetic penetration depths the induced current density and magnetic field intensity have been reduced to the exponential of -3 or only 5% of the surface values. The power per area [W/m^2] developed in the layer just slightly deeper than the third electromagnetic penetration depth, will be only 0.2% of the surface power density.

The electromagnetic penetration depths for 100% IACS copper (58 MS/m) and for 99.99% aluminium, with 65% IACS conductivity, have been plotted in Figure 2.6. At 50 Hz, the electromagnetic penetration depth of 11.6 mm into high purity aluminium is indicated by the dotted red lines. It can be seen clearly that the penetration depth becomes relatively negligible (say < 1 mm) at a frequency of about 6500 Hz for aluminium and 4000 Hz for copper.

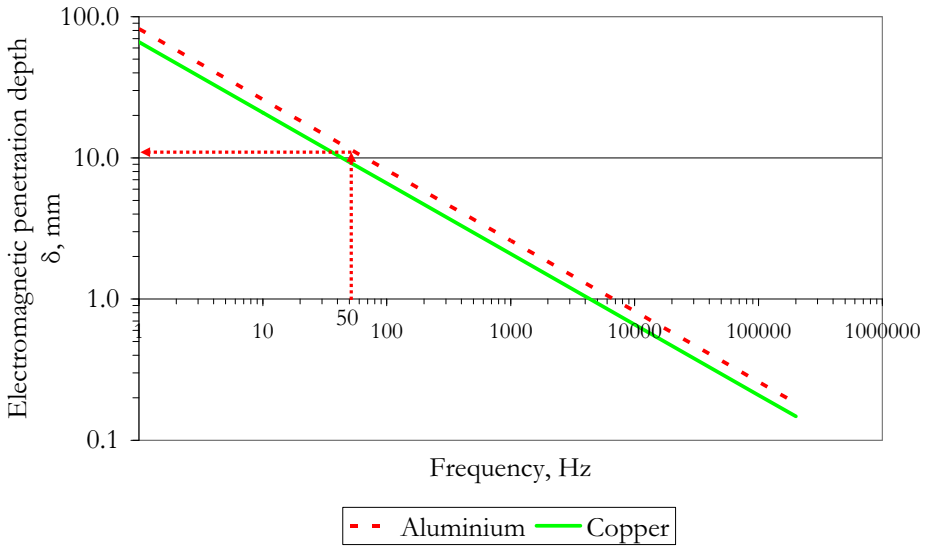

Figure 2.6-Electromagnetic penetration depth for 65% IACS aluminium (99.99% Al) and for 100% IACS copper.

For a high conductivity non-ferromagnetic materials (Copper, Aluminium, etc.), and particularly when operating at moderately high frequencies (say >4000 Hz), the flux is confined mainly to the first two electromagnetic penetration depths and is therefore virtually excluded from the 'bulk' of the coil copper and the work piece. The coil flux then becomes concentrated in the 'air-gap' between the coil and the work piece and the magnetic flux density increases as a result. This effect was indirectly described by Northrup [11] in his 'coupling factor' shown in Equation (50).

$$C = \left(\frac{D_w}{D_c} \right)^2 0.8 \tag{50}$$

where D_w is the outside diameter of the work piece and D_c is the inside diameter of the coil.

Northrup's value of C, is comparable in use to the square of the modified Nagaoka coefficient ($k^*_N{}^2$) shown previously in Equation (44). In 1945 Vaughan and Williamson proposed an empirically modified Nagaoka 'short-coil' correction factor based on their experiments conducted with 'high conductivity' non-ferromagnetic work pieces at 10 kHz as shown in Equation (51) [15].

$$k_N{}^* = k_N \left(1 - \left(\frac{D_w}{D_c} \right)^2 \right) + \left(\frac{D_w}{D_c} \right)^2 \tag{51}$$

Equation (51) is dealt with in each of the *Supplements*, and in most detail in *Supplement 3*. A summary is provided here. Equation (51) implies:

1. The coil and work piece are concentric cylinders, such that each can be defined by a single representative diameter.
2. The coil conductor is of square or rectangular section.
3. There is negligible penetration of the magnetic flux into both the coil and the work piece (a reasonable assumption at 10 kHz for large work pieces and coils as indicated in Figure 2.6).
4. The total amount of magnetic flux predicted for any given amount of current applied to the coil remains constant, (Equation (8) times the coil area), when a work piece is inserted into the coil interior.
5. The total magnetic flux is squeezed into the reduced coil-work piece 'air-gap', leading to a directly proportional increase in the magnetic flux density.
6. The change in the 'air-gap' length/area ratio does not change the total flux, i.e. the change in the magnetic reluctance of the interior of the coil has a negligible impact on the total amount of flux produced by a fixed amount of applied coil excitation current.

7. The magnetic flux density in the 'air-gap' is homogeneously distributed in the radial direction, i.e. the value at the surface of the work piece is the average value in the air-gap (this assumption is only approximately correct).
8. A completely 'full coil' has a 'short-coil' correction factor of 1, i.e. it behaves as a long coil. Equation (2) can therefore be used to adequately calculate the magnetic flux density of a coil with a negligibly small air-gap.
9. A large coil, with a negligibly small work piece, will behave as an 'air-core' coil and its magnetic flux density can be calculated using Equation (8). The intercept of Equation (53) at zero work piece diameter, is precisely the Nagaoka coefficient.

Equation (51) provides reasonable predictions of the heating of cylindrical loads, in cylindrical (helical) coils, at 50 Hz [21] (and will be confirmed based on the recent experimental results) and excellent results at high frequency (10 kHz), as per Vaughan and Williamson's original work [15]. It was postulated that the equation could however, be improved by the use of the electromagnetic penetration depth, as a means of correcting for the interaction of the electrical properties of the coil and work piece, and the frequency of the excitation current applied to the coil, as shown in Equation (52).

$$k_N^{\ *} = k_N \left(1 - \left(\frac{D_w - \delta_w}{D_c + \delta_c} \right)^2 \right) + \left(\frac{D_w - \delta_w}{D_c + \delta_c} \right)^2 \tag{52}$$

As Equation (52) remains semi-empirical (k_N, δ_w, and δ_c are analytical, and the volumetric correction empirical), it requires experimental verification to define its accuracy over a range of coil and work piece dimensions, work piece electrical conductivities and frequencies. The verification of Equation (52) through experiments and against a validated 2D axial symmetric FEM model is the primary focus of this work. Figure 2.7 provides a preliminary example of the impact of a high conductivity work piece on the magnetic field of a coil at low frequency in accordance with Equation (52).

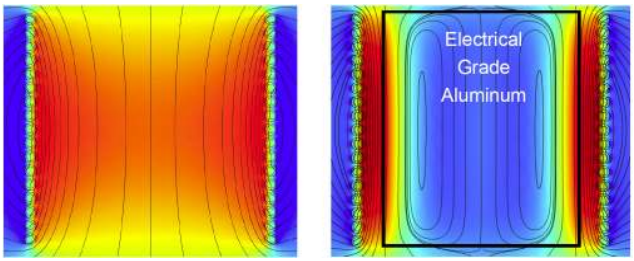

Figure 2.7-COMSOL 4.2® simulation showing the relative impact of the work piece on the magnetic flux density in the air-gap of a 'short coil' (17 turn), with both simulations using identical coil current and colour ranges, coil shape factor (D_{cs}/l_c) = 1.0, 50 Hz [*Supplement 1*].

Chapter 3

EXPERIMENTAL

3.1 Background

Induction heating of short segments of 'as cast' billets of different types were initially done as part of calibration exercises for a separate project [21, 30]. The billets were not completely regular in surface finish or diameter. A random selection of available alloys were initially used (1100, A356, 6053, 6082, 6060, 7108), and 'typical' electrical conductivity data, based on published results for various tempers, were assumed in that study.

The coils used in the preliminary study were designed specifically for use with high temperature liquid metal processing and were not optimized for billet heating experiments. Double and triple layer coils, imperfectly constructed and insufficiently supported long coils, or coils including non-axial symmetric ½ turns were available and therefore used [21, 30].

Initial heating experiments were conducted by cooling the work pieces in cold water and taking near 'instantaneous' readings over about 60 seconds, before the work pieces could heat from ~10°C to ~30°C.

During this 'learning phase' it was realized that the magnetic flux density was not as predicted by Equation (2) and that it varied along the length of the coil, as indicated in Figure 2.3. Measurements were then taken to estimate the variation of the magnetic flux density with length by measuring the turn-to-turn voltage drop, and deriving the magnetic flux density from the turn-to-turn inductance, as indicated in Figure 3.1 for a 16.5 turn coil (D/l=1.18), a 10.0 turn coil on a 10.8 kHz power supply (D/l=0.73) and a 41 turn coil (D/l=0.41). Note that D/l is taken as being equal to D_{cs}/l_c.

Comparison is made in Figure 3.1 with the centre-line flux density calculated using the Biot-Savart law, Equation (15), which should give a lower result than the measured values. The measured values should represent the average flux density over the

measured coil turns (a kind of radial integral). Please note that the long coil was constructed of two different pieces of copper, from different suppliers, and with different electrical conductivities (discontinuity between turns 8 and 10). Based on these measurements it was concluded that yes, the expected magnetic flux density variation according to Equation (15) did exist, but that this experimental methodology was not sufficiently accurate to study either 'air-core' coils or coils with work pieces to a precision worthy of publication.

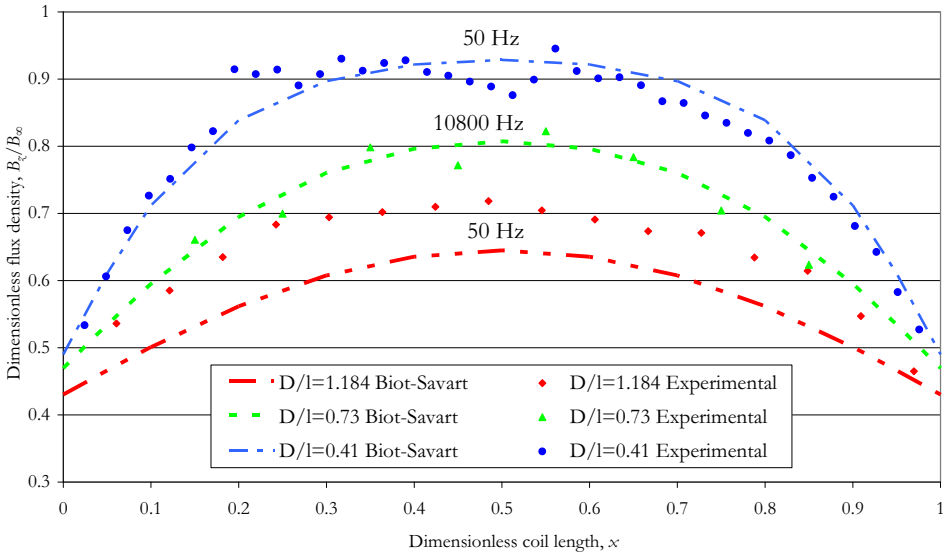

Figure 3.1- Initial measurements of the magnetic flux density variation with coil shape factor (D_{cs}/l_c) and comparison with the Biot-Savart law, Equation (15).

It was then decided to order new instrumentation, i.e. a high precision conductivity analyzer to determine the actual billet electrical conductivity (which was now known to vary significantly with casting conditions, subsequent heat treatment and aging), and a high accuracy Hall Effect Gauss meter to determine both the axial and transverse magnetic fields.

In order to obtain more control on the work piece physical dimensions and electrical properties, as well as steady state results and to prevent thermal damage to the Hall probes, machined and water cooled work pieces were constructed. New coils of precisely selected dimensions and 'full' number of turns, were constructed from the same roll of copper tubing to ensure consistent electrical properties. These coils were more carefully constructed using greater physical support, to try to obtain more ideal magnetic flux distributions.

3.2 Induction Heating Measurement [Supplements 1, 2 and 3]

The experimental approach is well documented in each of the attached *Supplements*. A summary will be provided here, with reference to the *Supplements* for additional information.

Experiments were conducted with 3 different work pieces having two different lengths and two different diameters (two constructed from 6060 and one of A356 aluminium alloy). Four different coils (three different diameters and two different lengths) were also constructed, resulting in a total of 7 combinations of work pieces and coils. High-Low experiments were conducted using different applied currents, to produce different magnetic flux densities and with different cooling water flow rates, to produce different operating temperatures and therefore work piece electrical conductivities.

The dimensions and properties of the machined work pieces and induction coils used in these experiments are summarized in Tables 2 and 3 [*Supplement 3*].

Table 2-Experimental Work Pieces [*Supplement 3*]

Work Pieces	**1**	**2**	**3**
Alloy	A356	6060	6060
Diameter, mm	75.0	95.0	95.0
Length, mm	130.0	130.0	260.0
Measured IACS Electrical Conductivity, %	48.4	56.2	53.4
Penetration depth δ_w (mm) at 50 Hz and 293 K from Equation (11)	13.43	12.47	12.79
ξ_R from Equation (28)	3.948	5.388	5.252
$\varphi(\xi_R)$ from Equation (43)	0.8244	0.8640	0.8607
Coil 1	1-1	1-2	
Coil 2	2-1	2-2	
Coil 3	3-1	3-2	
Coil 4			4-3

Table 3-Experimental Coils [*Supplement 3*]

Coils	Short Coil 1	Short Coil 2	Short Coil 3	Long Coil 4
Average Diameter, mm	132	142	155	132
Height, mm	106	109	108	218
Diameter to Height Ratio	1.24	1.30	1.44	0.60
Number of Turns	16	16	16	32
Short Coil Correction Factor from Equation (10)	0.641	0.630	0.607	0.786
Electrically Determined IACS Conductivity, %	80	80	80	80
Penetration depth δ_c (mm) at 50 Hz and 293 K	10.45	10.45	10.45	10.45
Total Length of Leads, cm	66	24	20	58
Coil Resistance at Maximum Current Including Leads, Ω	0.01047	0.01051	0.01157	0.02086
Coil Inductance, μH	26.38	29.08	33.39	61.93
Modified Nagaoka Coefficient k_N^* for Work Piece 1 from Equation (52)	0.720	0.700	0.669	
Modified Nagaoka Coefficient k_N^* for Work Piece 2 from Equation (52)	0.783	0.755	0.718	
Modified Nagaoka Coefficient k_N^* for Work Piece 3 from Equation (52)				0.870

Figure 3.2-Experimental work pieces #1 to #3, from left to right [*Supplement 3*].

Figure 3.3-32 turn 'long' induction coil #4, 132 mm average diameter, 218 mm long, (D_{cs}/l_c)= 0.60 [*Supplement 3*]. See Table 3 for details.

A schematic of the experimental apparatus used is shown in Figure 3.4 [*Supplement 3*].

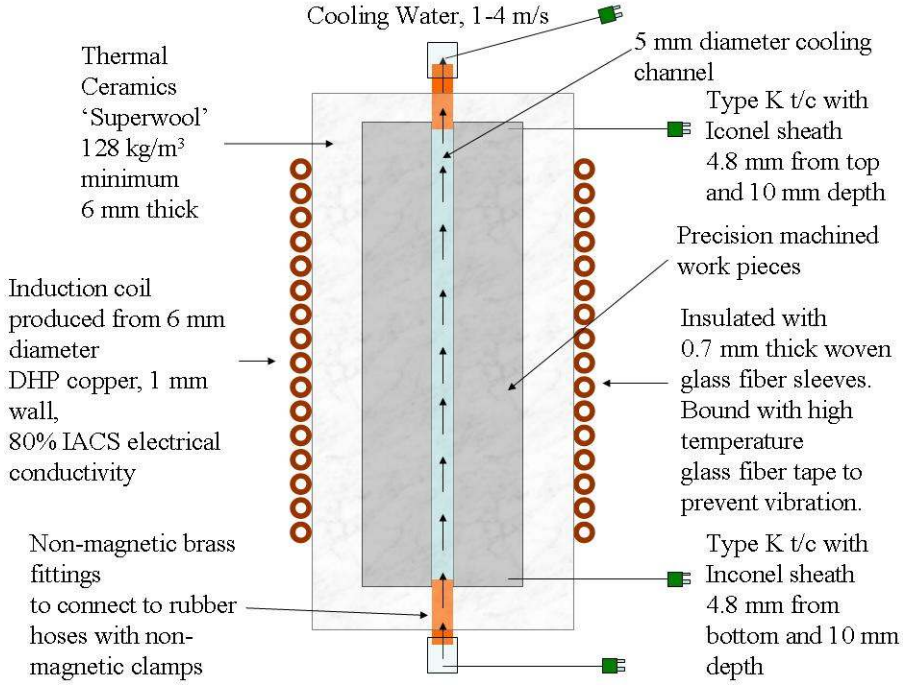

Figure 3.4-Schematic diagram of the water cooled, highly insulated billet heating apparatus [*Supplement 3*].

Work piece electrical conductivities were measured, using a General Electric Inspection Technologies, UK (AutoSigma 3000) conductivity analyzer to within ±0.5% accuracy, calibrated against aluminium standards (60.37% and 47.82% IACS). An arithmetic mean room temperature conductivity, based on 50-75 readings was estimated for each work piece.

Holes approximately 1 electromagnetic penetration depth deep (10 mm) were drilled, 4.8 mm from the top and bottom of each work piece (as shown in Figure 3.4), into which 1.0 mm diameter Type K thermocouples (with non-ferromagnetic Inconel sheaths) were press fit. The obtained temperature readings of the current carrying region of the work pieces, were used to provide reference temperatures for the calculation of the aluminium electrical conductivity for use in the analytical and FEM model heating rate prediction, and to calibrate the cooling channel heat transfer coefficient in the FEM model.

Power measurements (V, kA, kW, kVA, kVAr and power factor) were taken using a power quality analyzer from Fluke, USA (Fluke 43B), with a power measurement resolution of 0.1 kW. Coil current measurements were made with an inductive current probe from Fluke, USA (i1000S), with an accuracy of ±1% and a resolution of 1A.

Power was supplied by a simple transformer operating at line frequency (50 Hz) and delivering a nearly pure sinusoidal current to the system, with minimal harmonics as observed on the power quality analyzer.

Water flow rate was determined using weight and time, by data logging a scale which had a capacity of 100 kg and a resolution of 0.01 kg. The total weight difference over the period of each power reading was then used to calculate the average flow, which therefore had <0.1% error. One typical experimental set of data is shown in Figure 3.5, showing very clearly the steady state thermal period and the water flow rate measurement.

Measurements of the magnetic flux density were taken using a Pacific Scientific OECO, USA (F.W. Bell model 6010 Gauss meter) and were recorded manually. Standardized axial and radial Hall Effect probes, with a measuring error of less than ±1% for AC and ±0.25% for DC magnetic fields were used. The accuracy was confirmed using permanent magnet axial standards of 0.05034 T and 0.2003 T, and a transverse standard of 0.05054 T, prior to use of the probes. The agreement of probes with the supplied standards was found to be within the stated accuracy of the Gauss meter.

A series of High-Low billet heating experiments were conducted using the various coils and work pieces, as summarized in Table 4. A total of 11 conditions were tested, each with one duplicate, resulting in 22 separate sets of data.

Table 4-Summary of Billet Heating Experimental Conditions [*Supplement 3*]

Condition (#)	Coil (#)	Work Piece (#)	Current	Cooling Water Flow Rate
1	1	1	High	High
2	1	2	High	High
3	2	1	High	High
4	2	1	High	Low
5	2	2	High	Low
6	2	2	High	High
7	3	1	Low	High
8	3	1	High	High
9	3	2	High	High
10	4	3	High	High
11	4	3	High	Low

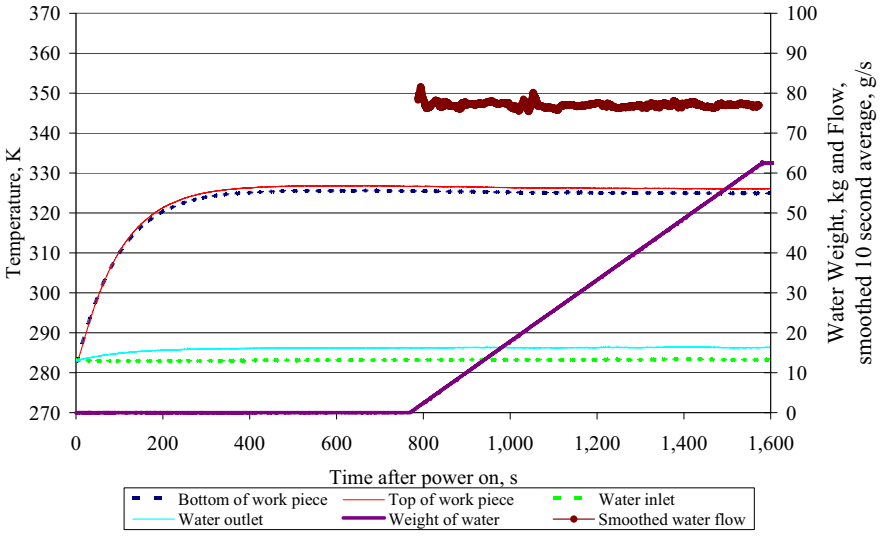

Figure 3.5-Typical data logged values for 'short' coil #1, and work piece #1, at high current (1028 A), 975 W heating and high water flow (76.7 g/s). A temperature gradient (bottom-top) can be seen from the cooling water inlet to outlet and a similar but smaller gradient can be seen on the 'hot face' [*Supplement 3*].

3.2.1 Electrical Conductivity [from Supplement 2]

In order to estimate the electrical conductivity or resistivity at the elevated operating temperatures of the experiments, Equations (53) to (55) are required. It is most convenient to work in resistivity units, as it results in a linear correlation with temperature as indicated by Equation (53):

$$\rho = \rho_o \left(1 + \alpha_{293}\left[T - 293K\right]\right) \tag{53}$$

where ρ is the resistivity of either the coil or the work piece, ρ_o is the resistivity of the metal at reference temperature T [Ω·m], α_{293} is the temperature coefficient of resistivity [K^{-1}], and T the reference temperature (293 [K]). The following values are recommended: for 100% IACS copper, ρ_o = 1.7241E-8 Ω·m (58.00 MS/m) and α_{293} = 0.00393 [28]. For 99.99% purity well annealed aluminium, ρ_o = 2.650E-8 Ω·m (65.0% IACS) and α_{293} = 0.0043 (for temperatures between 293 and 673 K) [36].

Electrical resistivity, ρ_o, of an alloy can be found from the measured %IACS conductivity by:

ρ_o for Alloy XXXX = ρ_o (for 100% IACS copper) * 100 / %IACS for Alloy XXXX (54)

For aluminium alloys, a new equation is proposed here based on comparison with available literature data [37-39], to estimate the temperature coefficient of resistivity:

$$\alpha_{293} \text{ for Alloy XXXX} = \frac{0.0043(Alloy XXXX\%IACS)}{65.0} \quad (55)$$

Combining Equations (53) through (55), the resistivity as a function of temperature of an aluminium sample can be estimated for temperatures between 293 and 673 K, from a single reading of %IACS conductivity measured at room temperature.

3.2.2 Calculation of Power and Heat Losses

In early experiments heating power had been determined by measuring the coil resistance at a thermal steady state, inserting a work piece and then multiplying the square of the new coil current with the work piece, times the change of the resistance as shown in Equation (56):

$$P_{electrical} = I^2_{with\ workpiece}(R_{with\ workpiece} - R_{without\ workpiece}) \quad (56)$$

where $P_{electrical}$ was the electrically determined power in [W].

This method assumes that the coil electrical resistivity did not change with and without a work piece. It was subsequently found that the electrical resistance of the coil varied with coil current, due to the constant cooling water flow rate. More current, created more heat, warmed the water more and resulted in a warmer and more resistive coil according to Equation (53). Changes of ±0.5 to 1 K were typical, causing a possible bias on the order of ±20-50W in the estimate of the work piece heating, depending on the coil, the coil current and the change in the coil current (magnitude of coil temperature change). The low resolution of power, while operating at over 500A (0.1 kW precision), combined with the changes in coil resistivity, resulted in the electrical method having both insufficient accuracy and precision. Based on the fact that multiple readings (typically 4 or 5) were used to produce average results, it is likely that these results included much less than the maximum possible precision error of 100 W. This would

lead to a total uncertainty of ~± 100 W on the electrical readings (not unreasonably high with 2000 W induced in the work piece, but very significant at low power, e.g. 500 W).

With the calorific heating measurement method, the heating rate (power) induced in the work piece was calculated from the cooling water flow rate, heat capacity and temperature change in accordance with Equation (57):

$$P_{calorific} = m_{water} C_p \Delta T \tag{57}$$

where $P_{calorific}$ is the calorifically estimated power [W], m_{water} is the mass flow rate of the water [g/s], C_p is the heat capacity of the water averaged from the inlet to the outlet temperature of the work piece [J/g/K], and ΔT is the change in temperature from the inlet to the outlet of the water cooled work piece [K].

As mentioned previously the mass flow of the water was measured with extremely high precision (<0.1% error) by using a high accuracy balance and high speed data logging. The heat capacity of water is known with very high precision and the arithmetic average was estimated using HSC version 4.1 [40] taking values at 0.1 K intervals. The dominating source of uncertainty in the estimation of the calorific heating rate was therefore the temperature differences in the thermocouples used to measure water in and out. These two thermocouples had been selected from a large batch of thermocouples, to give identical readings at room temperature, at 0.1 K resolution. A difference of more than 0.05 K would have resulted in a 'non-match'. In *Supplement 3* individual water ΔT values are recorded and 'water uncertainty' values have been calculated, which results in ±0.05 K becoming an average uncertainty of ±1.7%.

In the modelling of the experiments, the work pieces are assumed to be 'perfectly' insulated. High quality, Thermal Ceramic's 'Superwool' [41], (128 kg/m^3 and 6 mm thick) was used to insulate the work pieces. Where possible double or even triple layers of insulation where used (smaller work pieces inserted into larger diameter coils). Work piece heat losses were then estimated by considering in each case the actual thickness of wool used and the average 'hot face' temperature given by the imbedded thermocouples as shown in Figure 3.4. The 'cold face' of the insulation was assumed to be at ambient temperature in order to estimate the maximum heat losses according to Equation (58). In *Supplement 1*, the average value of the heat losses was reported to be 0.4%.

$$P_{loss} = \frac{k_{wool}}{d_{wool}} A_w \left(T_{average\ Al} - T_{ambient} \right) \tag{58}$$

where P_{loss} are the heat losses [W], k_{wool} was the thermal conductivity of the ceramic fibre insulating blanket (typical value of 0.02 [W/m/K] at the work piece operating temperature), d_{wool} was the actual thickness of the wool used for each experiment [m], A_w was the total area of the work piece [m^2], $T_{average\ Al}$ was the average temperature recorded

by the two imbedded thermocouples [K] and $T_{ambient}$ was the typical room temperature [293 K].

3.3 Magnetic Flux Density Measurement [Supplements 2 and 3]

A number of measurements have also been taken to determine the variation of the magnetic flux density, both radially and axially within the 'air-gap' volume of the experimental coils, with and without work pieces. This experimental data is intended to provide additional validation of predictions made using analytical equations, e.g. Equation (15), and numerical methods, i.e. 2D axial symmetric FEM.

Measurements were made for 'short' Coil #1 both empty and with Work pieces #1 and #2 and for 'long' Coil #4 with and without Work piece #3. As the axial Hall Effect probe had a 'finite' diameter of 6 mm, results near the coil wall and near the work pieces, have been plotted allowing for the average off-set in the readings taken, i.e. 3 mm. Centre-line readings were of course taken with the probe aligned as perfectly as possible on the exact central axis of the coil. See *Supplements 2* and *3*, for further details.

Magnetic flux measurements were also made over the top of the 'air-core' of Coil #1 and outside of Coil #1 in a radial direction, using the transverse Hall Effect probes. Results will be compared with the predictions made using the validated FEM model. It was necessary to carefully account for the thickness of the probe, the thickness of the support used (a plastic ruler) and any height off-set. The same off-set was applied in the calculation of the 2D axial symmetric FEM estimates used for comparison.

Chapter 4

RESULTS AND DISCUSSION

4.1 Heating Experiments [Supplements 1 and 3]

The main results of the heating experiments are shown in Table 5 and Figure 4.1, taken from *Supplement 3*. See also *Supplement 1* for further details.

Table 5-Summary of Billet Heating Experimental Results [*Supplement 3*]

Condition	Heating Power Calorific (W)	Heating Power Electrical (W)	Electrical Calorific Absolute Difference (%)	Heating Power FEM (W)	FEM Calorific Absolute Difference (%)	Heating Power Analytical Equation (52) (W)	Analytical Calorific Absolute Difference (%)	Heating Power Analytical Equation (51) (W)	Analytical Calorific Absolute Difference (%)
1-A	636	631	0.9	623	2.1	659	3.6	732	15.1
1-B	634	611	3.6	623	1.7	659	3.9	732	15.5
2-A	975	N/A	N/A	976	0.1	1035	6.1	1167	19.7
2-B	954	1019	6.8	970	1.6	1029	7.9	1161	21.6
3-A	544	558	2.5	537	1.4	571	5.0	629	15.6
3-B	543	578	6.5	536	1.3	570	5.0	627	15.5
4-A	536	623	16.3	541	1.0	576	7.6	637	18.9
4-B	534	592	10.8	542	1.5	577	8.1	638	19.5
5-A	813	926	13.9	840	3.2	888	9.1	994	22.2
5-B	811	926	14.2	840	3.6	888	9.5	994	22.6
6-A	798	885	10.9	825	3.4	873	9.4	974	22.1
6-B	795	885	11.3	824	3.7	872	9.7	974	22.5
7-A	411	506	23.1	399	2.9	432	5.1	473	15.1
7-B	407	523	28.4	398	2.3	431	5.8	472	15.9
8-A	518	605	16.9	508	1.9	549	6.1	602	16.4
8-B	520	610	17.3	508	2.2	549	5.8	602	16.0
9-A	642	688	7.2	618	3.7	658	2.5	729	13.5
9-B	643	703	9.2	617	4.1	657	2.2	728	13.1
10-A	1884	2117	12.3	1888	0.2	1911	1.4	2042	8.4
10-B	1894	2132	12.6	1881	0.7	1903	0.5	2034	7.4
11-A	746	732	1.8	713	4.4	721	3.2	769	3.2
11-B	736	727	1.2	713	3.0	722	1.9	770	4.6
		Average:	10.8	Average:	2.3	Average:	5.4	Average:	15.6

Table 5, clearly shows that the electrical measurement method without 'coil temperature compensation' or 'coil temperature control', e.g. through the use of external baths of coolant, is not sufficiently accurate for scientific work. The FEM model has an 'error' of less than 2%, when the impact of the unaccounted heat losses is considered. The analytical model using the improved frequency corrected short coil correction factor,

Equation (52), has an error of ~5% on average, with a range from nearly zero to 10%, indicating that the magnetic field at the surface of the work piece, has been estimated to an accuracy of ~2-3%. The non-frequency corrected Equation (51) has an error three times as large as the frequency corrected Equation (52), showing the improved effectiveness of the modified equation at low frequency.

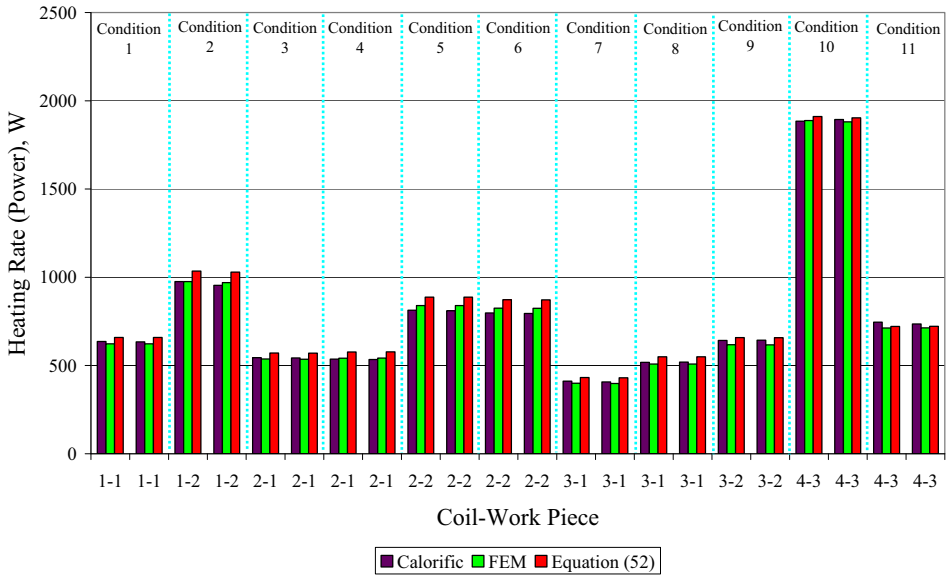

Figure 4.1-Main results of induction heating experiments, comparison of calorific measurements with 2D axial symmetric FEM and analytical model calculations [*Supplement 3*].

The error and uncertainties in the thermal analysis are discussed in detail in *Supplement 1*. In Figure 4.2, the effect of the assumption of 'homogeneous' aluminium temperature implicit in assuming one 'representative' temperature to evaluate the electrical resistivity via Equation (53) has been assessed.

As explained in *Section 2.3*, current and therefore power is highly concentrated into the outermost couple of electromagnetic penetration depths. The very low temperatures or indeed the presence of the cooling channel at the centre of the billet, shown in Figure 4.2, therefore had virtually no impact on the heating rate (~1 W magnitude), while the temperature gradients in the rest of the work piece introduced errors of <0.5% based on FEM models solved with temperature variable properties, ie. Equations (53) through (55). The two measured temperatures at a depth of approximately 1 electromagnetic penetration depth, were therefore 'representative' of the average temperature and hence appropriate for the estimation of the electrical resistivity of the current path.

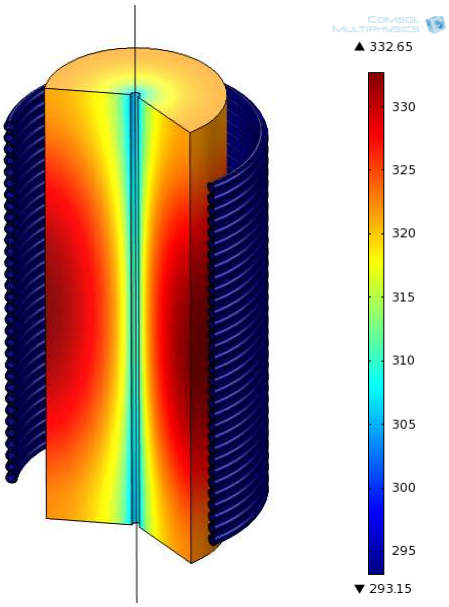

Figure 4.2-Temperature distribution, K, in work piece #3, for the 'long' coil #4 at 892.6 A and 50 Hz (condition 10 average), assuming perfect thermal insulation at steady state. Note the temperature scale of 293 K – 333 K (20-60 °C).

4.1.1 High Frequency Heating Estimates from FEM and Analytical Models [Supplements 1-2]

The experimental equipment used in this study operated with the line frequency of 50 Hz. It would have been possible to run experiments with other coils, at other frequencies, but due to the small area available for cooling on the interior of the work pieces, it was not practical to operate with higher input powers. Transition to film boiling and work piece overheating would have resulted. Instead 'virtual' experiments were executed comparing experimental data at 50 Hz, and model data from 50 Hz to 500 kHz as shown in Table 6, using both the analytical and 2D axial symmetric FEM models.

The FEM model had been created initially as part of another research effort and the development and validation is dealt with in detail elsewhere [42]. *Supplement 2* summarizes the pertinent aspects of the FEM model to this work.

Data for use in the modelling have been taken from *Supplement 3* Appendix Tables I and II. The results for the 'short' Coil #1, Work piece #1, Condition #1 (1001.0 A) are

shown in Table 6 below. Additional results for the long Coil #4 and discussion can be found in *Supplement 2* (Table III).

Table 6-Comparison of Experimental, Analytical (Equation 52) and FEM Model Heating Rate (Power) Results for Short Coil #1, Work Piece #1 and Condition #1 [*Supplements 1-2*]

Frequency (Hz)	Calorific Experimental Power (W)	Electrical Experimental Power (W)	Analytical Power Equation (52) (W)	FEM Power (W)	Analytical-FEM Difference (%)
50	634	611	659	623	5.8
500	N/A	N/A	2567	2466	4.1
5000	N/A	N/A	8672	8370	3.6
50000	N/A	N/A	27957	26816	4.3
500000	N/A	N/A	88623	85247	4.0
				Average:	4.3

In Table 6, it can be clearly seen that the difference between the model results, from 50 Hz to 500 kHz, is nearly independent of frequency. This implies that any bias due to the use of Equation (52), compared to the 2D axial symmetric model, is consistent, and that the use of the equivalent 'current sheet' diameter in Equation (52), appears to give valid heating estimates over a wide range of frequencies. The heating power calculated by both the analytical and FEM models, exhibits the expected frequency dependence, i.e. $P_w \propto \sqrt{f}$, at over 500 Hz, i.e. $\xi_R>5$ (see Figure 2.5). See *Supplements 1-3* for further discussion.

Agreement is better between the FEM and analytical results for the long Coil #4, with an average difference of only 0.8% (see *Supplement 2*). Consistent agreement is again found between the models as a function of frequency. The long coil is more 'ideal' (k_N closer to 1.0) and hence Equation (52) applies less correction. Errors introduced by the semi-empirical nature of Equation (52) are therefore of lower magnitude. In addition, the lower radial variation in the magnetic flux density of the longer coil, means that the magnetic field at the surface of the work piece should be closer to the 'average' air-gap magnetic flux density, i.e. the value which is effectively predicted using Equation (52). See *Supplement 2* for further discussion.

The radial gradient of the magnetic flux density for the short Coil #1 is shown in Figure 4.3, for 'lines' evaluated in COMSOL® taken from the side of the work piece, passing between the coil turns, terminating at a radius equal to the outer radius of the coil turns, and evaluated at the indicated dimensionless coil lengths, x. It can be seen that there is less radial gradient in the middle of the coil (x=0.5) than near the end (x=0.125). The prediction from Equation (52) for Coil #1 with Work piece #2 is plotted at 50 Hz (k_N^*=0.783), showing good agreement with the typical magnitude of B_z/B_∞ at the surface of the work piece predicted by the FEM model.

At 500 kHz, the reduced electromagnetic penetration depth into the work piece, results in an increase in the predicted average magnetic flux density at the surface of the work piece (k_N^*=0.828) using Equation (52), and a similar change in magnitude is indicated for x=0.125, at 500 kHz from the FEM model.

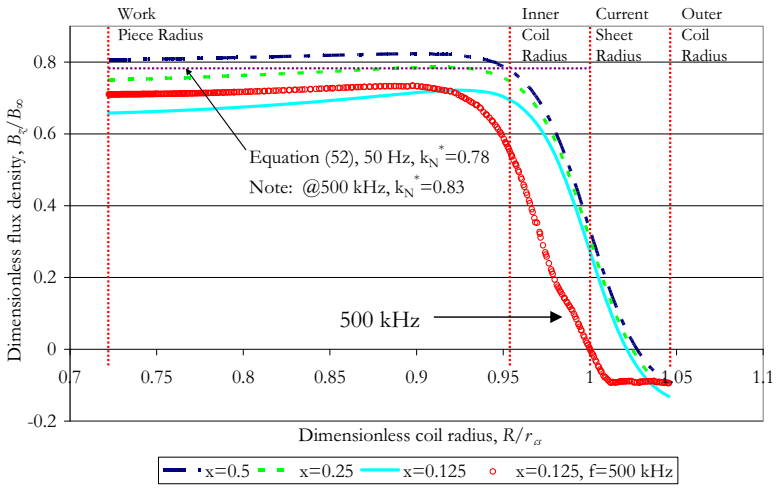

Figure 4.3-Dimensionless flux density as a function of dimensionless radial position (R/r_{cs}) for short coil #1 and work piece #2 at 50 Hz and 500 kHz, for various dimensionless axial positions (x). The gradient is evaluated along a line that is drawn to pass between adjacent coil turns (i.e. in the gap between turns).

Figure 4.3 also shows that the flux shifts to the inside of the coil at high frequency (500 kHz shown as an example), resulting in both different flux densities in the coil air-gap, and 'effective' coil diameters. The 'effective' high frequency coil diameter could be defined as the diameter that results in the correct estimate of coil inductance or total lines of magnetic flux, assuming a homogeneous average flux density given by Equation (8), e.g. for an 'air-core' coil: $\Phi_z = B_z A_c = k_N B_\infty \pi D^2_{effective}/4$.

The high frequency behaviour of coils is the result of the complex interaction of several factors including the:

- coiling of the conductor (flux concentrated in the 'air-core' of the coil),
- skin effect (frequency, electrical conductivity), and
- proximity effect (frequency, coil tube shape and spacing), and the
- resulting impact on both the coil's local resistance (change in current distribution) and inductance.

The high frequency resistance and current distribution have been explored both analytically and using FEM elsewhere [42]. Considerable analytical analyses and experimental data are available in the literature on this topic [43-59].

The impact of frequency on coil 'air-core' or 'empty-coil' inductance has been estimated using the FEM model for the long Coil #4 and found to vary from 60.46 μH at 50 Hz, to 57.58 μH at 500 kHz (i.e. a change of 4.8%), indicating a reduction in the 'effective' coil diameter at high frequency. The FEM calculated inductance for 'air-core' short Coil #1 as a function of excitation frequency is plotted in Figure 4.4, indicating a change of 5.9%. See Figure 12 of *Supplement 3* for further details.

The good agreement shown in Table 6 and in Table III of *Supplement 2*, imply agreement of the predicted average flux density at the surface of the work piece, as a function of both current and frequency, and not necessarily agreement for the overall average flux density or the resulting coil inductance, i.e. between the assumed vs. 'actual' equivalent coil diameters at different frequencies.

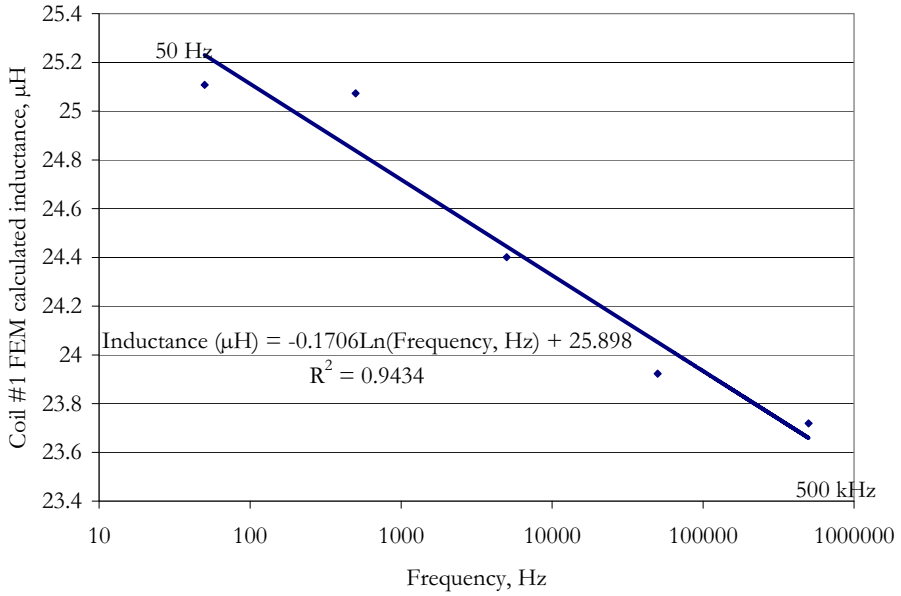

Figure 4.4-Short Coil #1, 2D axial symmetric FEM model calculations of 'air-core' inductance as a function of coil current frequency.

The effect of frequency on coil magnetic flux distribution in the 'near coil region' is shown in Figure 4.5. The flux moves to the inside of the coil and reduces in density very strongly between the coil turns due to the increase in proximity effect, thus the non-ideal

tubular nature of the coil (*it really is not a current sheet*), is more apparent in the magnetic flux density distribution at high frequency, as compared to low frequency.

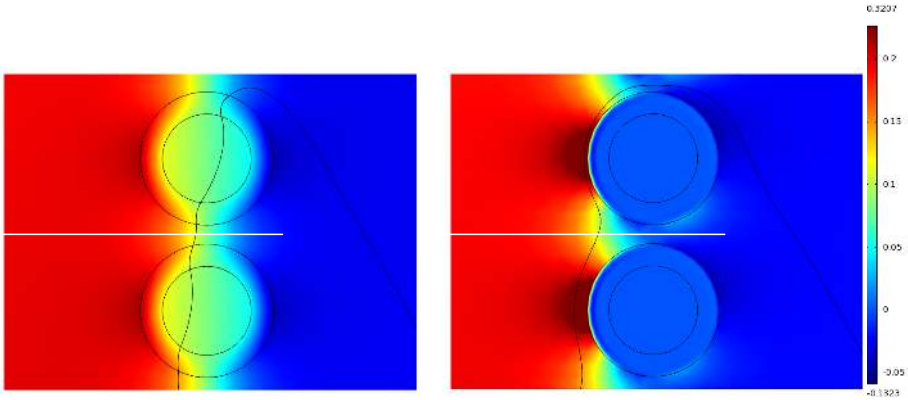

Figure 4.5-Peak flux density ($B_{\tilde{z}}$[T]), at constant current for 50 Hz (left) and 500 kHz (right), for long Coil #4 at x=~0.25. The white line indicates the approximate path drawn in Figure 4.3 at x=~0.25. δ_c = 10.5 mm at 50 Hz and 0.1 mm at 500 kHz. Tubing is 1 mm thick and 6 mm in diameter.

4.2 Verification of Frequency Modified Short Coil Correction Factor, Equation (52), via Inductance and Reactive Power [Supplement 3]

During the execution of the heating experiments the reactive or 'imaginary' power of the 'air-core' coils and of the coils with work pieces, were also measured. The relationship between reactive power, reactance and inductance is given by Equations (59) and (60), ignoring the inductance of the 'leads'.

$$Q_{total} = Q_w + Q_{airgap} + Q_c \tag{59}$$

where Q_{total} is the total reactive power measured at the leads of the coil [VAr], Q_w is the reactive power of the work piece estimated from Equation (46) [VAr], Q_{airgap} is the reactive power induced in the coil, due to the flux in the air-gap [VAr] and Q_c is the reactive power due to the magnetic flux inside the conductors of the coil itself [VAr].

If a current sheet approximation is used then Q_c=0 and the diameter of the equivalent current sheet can be used to estimate the Q_{airgap} using Equation (60):

$$Q_{airgap} = I_c^{\,2} X_{airgap} = I_c^{\,2} 2\pi f\ L_{airgap} = I_c^{\,2} 2\pi f\ L_c \left(\frac{D_{cs}^{\,2} - D_w^{\,2}}{D_{cs}^{\,2}} \right) \frac{k_N^*}{k_N} \tag{60}$$

where I_c is the coil RMS current [A], X_{airgap} is the inductive reactance [Ω] caused by the magnetic flux in the air-gap linking with the coil turns, f is the frequency of the current [Hz], L_c is the 'air-core' inductance [H] calculated from the measured 'air-core' reactive power or the calculated 'air-core' inductance using Equations (6) or (9), k_N^* is the modified short coil correction factor given by Equation (52), and k_N is the Nagaoka coefficient given by Equations (7) or (10), D_{cs} is taken as the equivalent 'current sheet' diameter [m], and D_w is the work piece outer diameter [m]. Equation (60) is only valid for full electromagnetic penetration of the coil, i.e. at low frequency such as at the 50 Hz used in the experimental program described in *Supplement 3*.

Both Equations (46) and (60) utilize the new frequency modified short coil correction factor, Equation (52). Comparing the calculated to the measured reactive power, therefore offers an independent experimental means of verification of the accuracy of the new Equation (52), i.e. without reference to work piece heating, or measured coil electrical resistance. Reactive power measurements will be nearly independent of temperature over limited ranges.

For the short Coil #1, the 'air-core' coil inductance including the current supply leads, calculated from the measured current and reactive power was 26.38 μH (average of 25 readings) and the inductance of the coil estimated using Equation (9) was 26.41 μH. For long Coil #4, the measured value was 61.93 μH (average of 21 readings) and the calculated value was 62.88 μH. Therefore the differences were less than 2% between the calculated and measured coil 'air-core' inductance values. It should be noted that the coil current is used in the calculation of the 'measured' inductance and that the Fluke i1000s current clamp had a maximum uncertainty of 1%, which is squared in the error term (i.e. 2% maximum measurement error), leading to the conclusion that there are no significant differences between the measured and the calculated inductances for the air-core coils. Lead compensation was not applied, as lead length was minimal and the magnitude insignificant when compared to the uncertainty in the current measurement. Rosa's round coil correction factor was also not applied, due to the use of hollow tubing [*Supplement 3*].

Using the inductances of the air-core coils as listed in Table 3, and Equations (46), (59) and (60), and comparing with the measured reactive power (VAr) for short Coil #1 with a work piece, resulted in an average absolute error of 0.94%. For long Coil #4, the result was an average error of 0.75%. It is therefore concluded that the reactive power measurements are in excellent agreement with the magnetic flux density and induction heating calculation methodology presented in this document, i.e. Equation (52). Results of these calculations are summarized for all of the experimental conditions in Table 7 and are plotted in Figure 4.6. Overall a typical difference of 0.84% is calculated for all coils and work pieces measured at 50 Hz [*Supplement 3*].

The excellent agreement found using Equation (60) implies that Equation (52) correctly predicts the average flux density in the air-gap between the coil and the work piece. This strongly supports the hypothesis that the positive bias, resulting from the use of Equation (52) in the estimation of the heating rate of the work piece (~+5% on average as shown in Table 5), is due to radial gradient of the z-component of the magnetic flux across the air-gap, as shown in Figure 4.3.

Table 7-Summary of Billet Reactive Power Results

and Comparison with Analytical Estimates [see *Supplement 3* for further details]

Condition	Reactive Power (kVAR)	X_I Inductive Reactance (Ω)	Inductance (μH)	Short Coil Correction Factor Equation (10) (k_N)	Modified Short Coil Correction Factor Equation (52) (k^*_N)	Air-Gap Fraction Air Equation (60)	Air Gap Inductance Equation (60) (μH)	Air Gap Reactive Power Equation (60) (VAR)	Work Piece Reactive Power Equation (46) (VAR)	Total Calculated Reactive Power Equation (59) (VAR)	Absolute Error (%)
1-A	7.2	0.00718	22.86	0.641	0.719	0.67	19.96	6286	816	7102	1.36
1-B	7.2	0.00719	22.87	0.641	0.719	0.67	19.96	6283	816	7098	1.41
2-A	6.3	0.00599	19.07	0.641	0.780	0.48	15.34	5103	1216	6319	0.37
2-B	6.3	0.00599	19.07	0.641	0.780	0.48	15.35	5069	1206	6275	0.39
3-A	7.7	0.00813	25.87	0.630	0.699	0.72	23.24	6917	707	7624	0.99
3-B	7.6	0.00807	25.70	0.630	0.699	0.72	23.24	6903	705	7608	0.33
4-A	7.6	0.00816	25.97	0.630	0.698	0.72	23.20	6790	726	7516	1.11
4-B	7.6	0.00815	25.95	0.630	0.698	0.72	23.20	6793	727	7521	1.04
5-A	6.9	0.00701	22.32	0.630	0.752	0.55	19.14	5918	1047	6965	0.94
5-B	6.9	0.00701	22.32	0.630	0.752	0.55	19.14	5918	1047	6965	0.95
6-A	6.9	0.00698	22.23	0.630	0.754	0.55	19.18	5952	1023	6975	1.08
6-B	6.9	0.00698	22.23	0.630	0.754	0.55	19.18	5952	1022	6974	1.08
7-A	7.4	0.00962	30.63	0.607	0.668	0.77	28.14	6784	535	7319	0.87
7-B	7.3	0.00955	30.40	0.607	0.668	0.77	28.14	6758	533	7292	0.11
8-A	9.3	0.00961	30.60	0.607	0.668	0.77	28.12	8548	686	9234	0.71
8-B	9.3	0.00962	30.61	0.607	0.668	0.77	28.12	8544	686	9230	0.75
9-A	7.1	0.00858	27.32	0.607	0.717	0.62	24.64	6402	769	7172	1.01
9-B	7.1	0.00860	27.36	0.607	0.717	0.62	24.64	6393	768	7161	0.85
10-A	10.5	0.01315	41.86	0.786	0.869	0.48	32.70	8202	2253	10455	0.43
10-B	10.5	0.01314	41.83	0.786	0.869	0.48	32.70	8169	2245	10414	0.34
11-A	4.0	0.01294	41.18	0.786	0.870	0.48	32.74	3200	846	4045	1.14
11-B	4.0	0.01285	40.89	0.786	0.870	0.48	32.74	3203	846	4049	1.22
										Average	0.84

The measurement precision on the reactive power, was 0.1 kVAr, as indicated in Table 7. This represents a typical uncertainty of ±0.7% based on the average measured magnitude of the reactive power. This would indicate that the average observed 'error' is virtually identical to the measurement uncertainty.

It is a reasonable assumption that for high frequencies, Equation (60) should be evaluated substituting the inner coil diameter and electromagnetic penetration depth ($D_c+\delta_c$) for the current sheet diameter (D_{cs}), as the best available estimate of the 'effective high frequency diameter'. Alternatively the contribution from the true air-gap can be separated from the high frequency coil reactive power, as discussed in detail in *Supplement 3,* as a function of frequency.

Applying the more comprehensive methodology presented in *Supplement 3,* it is possible to analytically solve for the system reactance as a function of frequency and this in turn can be compared to similar FEM models, as shown for short Coil #1 and Work piece #1 in Table 8.

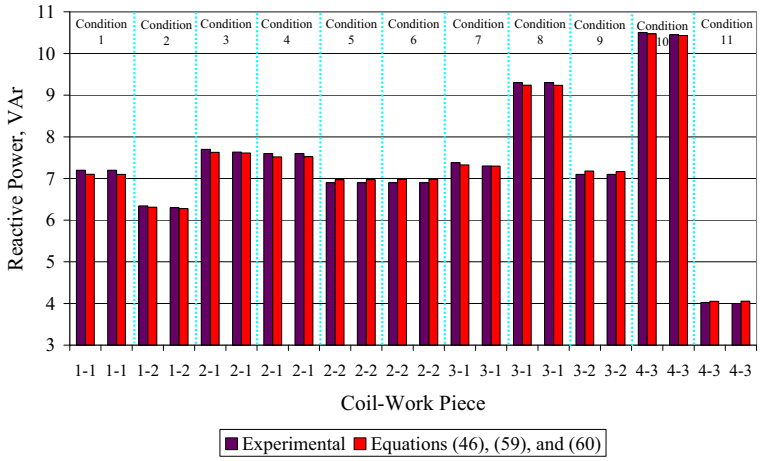

Figure 4.6-Experimental and calculated system reactive power [*Supplement 3*].

Results in Table 8 are 'pure' model vs. model results, with Equation (6) being used to estimate the air-core inductance, resulting in a larger average difference (3.7%) when compared to the low frequency modelling shown in Table 7 (0.84%), which make use the measured air-core results at 50 Hz. Better results are obtained for a long coil as shown in Table VI of *Supplement 3,* and as would be expected based on the previous discussion in Section 4.1.1.

Table 8-'Short' coil #1, Work Piece #1, Condition #1
Total System Reactive Power, VAr
(1001.0 A, Coil conductivity 4.3*107 S/m) [*Supplement 3*]

Frequency (Hz)	Electrical Reactive Power (VAr)	Analytical Reactive Power (VAr)	Electrical-Analytical Difference (%)	FEM Reactive Power for round wire (VAr)	Analytical-FEM Difference (%)
10	N/A	1.53E+03		1.54E+03	0.8
20	N/A	2.99E+03		2.95E+03	1.4
35	N/A	5.06E+03		4.91E+03	3.0
50	7.20E+03	7.12E+03	1.09	6.83E+03	4.1
500	N/A	6.50E+04		6.22E+04	4.2
5000	N/A	6.10E+05		5.82E+05	4.5
50000	N/A	5.97E+06		5.63E+06	5.6
500000	N/A	5.93E+07		5.56E+07	6.2
				Average:	3.7

4.3 Magnetic Flux Density Measurements [Supplements 2 and 3]

Results from the magnetic flux density measurements are dealt with in detail in *Supplements 2* and *3*. A summary of the main results will be provided here, with additional FEM model validation data not previously reported in the *Supplements*.

'Air-core' results are shown for Coil #1 in Figure 4.7. Magnetic flux densities measured for Coil #1 with an 'air-core' and with Work piece #2, are shown in Figure 4.7. Figures 4.7 and 4.8 clearly show the axial variation of the z-component of the magnetic flux density as expected from Equation (15). Figure 4.7 also clearly indicates the expected radial distribution of the z-component expected for a 'short-coil'. Magnetic flux density is highest near to the coil tubing, and lowest on the coil centre-line. Accurate readings near to the coil tubing were difficult to obtain, due to small imperfections in the coil stacking. The 2D axial symmetric model results clearly show the local variations in the magnetic flux density caused by the round coil tubing.

The Nagaoka coefficient (k_N =0.641) is drawn on Figure 4.7. k_N represents a double integral of the z-component of the dimensionless flux density, i.e. the average of infinite number of readings in both the x and r directions, all the way to the 'current sheet diameter', which physically exists inside the coil tubing and can thus not be measured. An average of the available experimental data sets, fortuitously gives an average dimensionless z-component flux density value of 0.64.

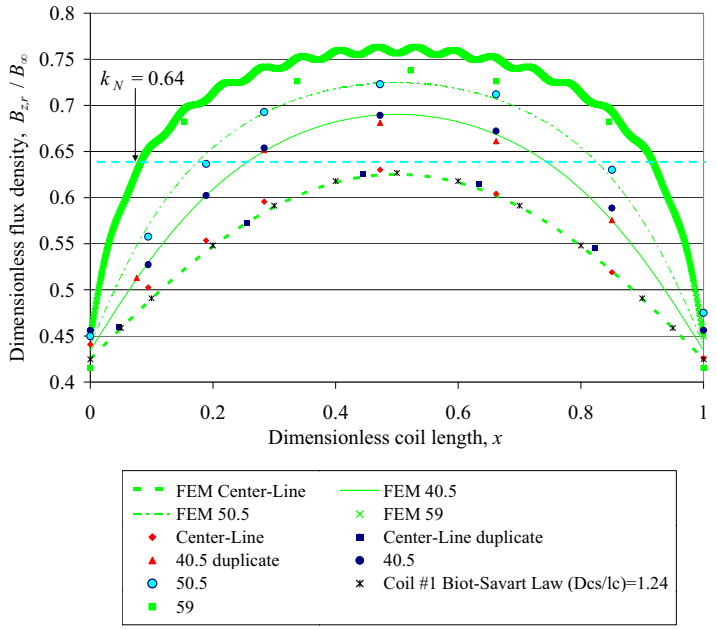

Figure 4.7-Dimensionless flux density (z-component) as a function of dimensionless coil length and radial position [mm] for 'air-core' coil #1, comparison of measured, analytical and FEM results [*Supplement 3*].

Near perfect agreement is found on the centreline of Coil #1, between the experimental values and the results of Equation (15) for the z-component of the magnetic flux density (B_z), supporting the use of the 'equivalent current sheet diameter' in Equations (52) and (60). Predictions from the 2D axial symmetric FEM model, are also identical, providing strong validation for the numerical model.

Results from duplicate measurements in Figure 4.7 and 4.8 show good reproducibility. Agreement with the axial symmetric FEM model is about 1%, except near the ends of the coil (and near to the coil windings), which may be due to the fact that a helical coil with current supply leads is only approximately 'axially symmetric'. In an axial symmetric model, the coil is modelled as a series of 'perfectly horizontal stacked current rings', as explained in *Supplement 2*, so exact agreement, particularly near the ends of the coils, should not be expected.

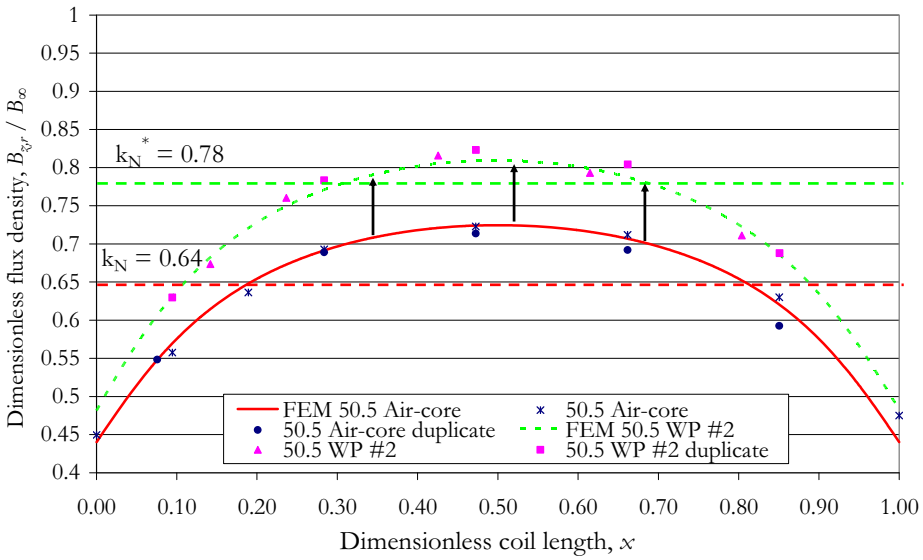

Figure 4.8-Dimensionless flux density (z-component) as a function of dimensionless coil length for 'short' coil #1 with 'air-core' and with work piece #2, comparison of measured and FEM results at 50.5 mm radius [*Supplement 3*].

Figure 4.8 indicates an increase in the air-gap magnetic flux density caused by the presence of the work piece, as expected from Equation (52). Additional results are given in Figure 4.9 (Work piece #1 and Coil #1) and Figure 4.10 (Work piece #3 and Coil #4). The larger diameter Work piece #2 resulted in a greater increase (~37%) in the magnetic flux density in the air-gap of Coil #1, as compared with Work piece #1 (~21%), again as expected from Equation (52). The longer Coil #4 has a larger initial 'air-core' Nagaoka coefficient (0.79) and only a 10% increase (0.87) in the presence of

Work piece #3. For Coil #4 agreement between the analytical estimates, FEM and experimental results are excellent both on the centreline and at the work piece radius, due to the more 'ideal' nature of the long coil (more homogenous flux distribution) and lesser magnitude of correction required from Equation (52).

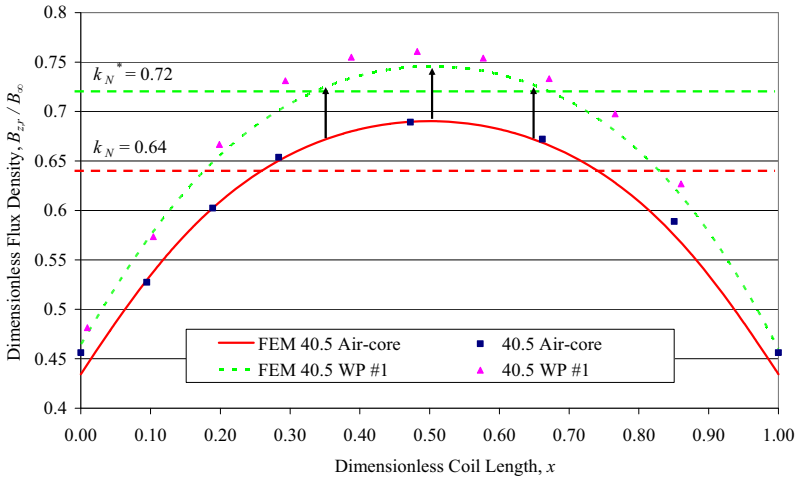

Figure 4.9-Dimensionless flux density (z-component) as a function of dimensionless coil length for 'short' coil #1 with 'air-core' and with work piece #1, comparison of measured and FEM results at 40.5 mm radius.

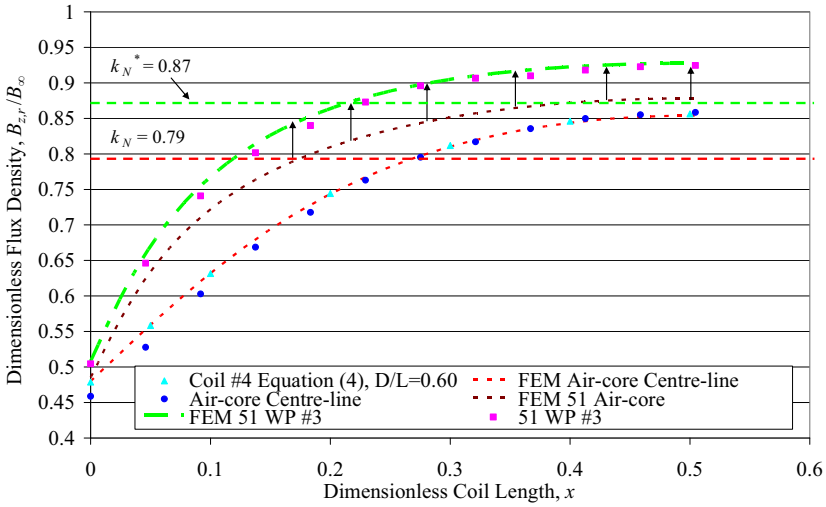

Figure 4.10-Dimensionless flux density (z-component) as a function of dimensionless coil length and radial position (center-line and 51 mm) for 'long' coil #4 'air-core' and with work piece #3, comparison of measured, analytical and FEM results.

Additional measurements were taken during the validation phase of the 2D axial symmetric FEM model development, which have not been reported elsewhere. Measurements were taken using the transverse Hall Effect probe, 3 mm over the top of the coil, with the probe supported on a plastic ruler. As the coil is longer on one side than on the other, one would expect to see a radial bias in the magnetic flux density, when compared with 2D axial symmetric models, which assume flat coil turns, as can be seen from the experimental data shown in Figure 4.11.

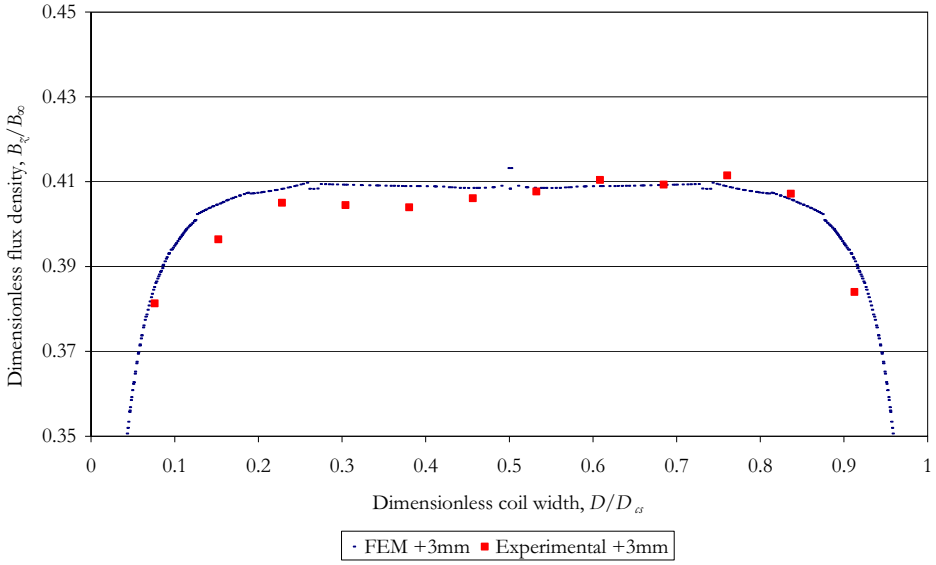

Figure 4.11-Comparison of measurements at 3 mm over and across the 'air-core' of short coil #1, with 2D axial symmetric FEM modelling results.

The absolute value of the dimensionless magnetic flux density is shown in Figure 4.12 as a function of radial position measured outwards starting from the equivalent 'current sheet diameter' (D_{cs}), measured at -5 and -10 mm under the elevation of the coil. Absolute magnitudes of the FEM results are indicated, as the experimental results are magnitudes only (i.e. the Hall Effect probe on AC can not indicate a direction). Excellent agreement was again obtained between the axial symmetric FEM and measurements, further validating the overall accuracy of the modelling approach.

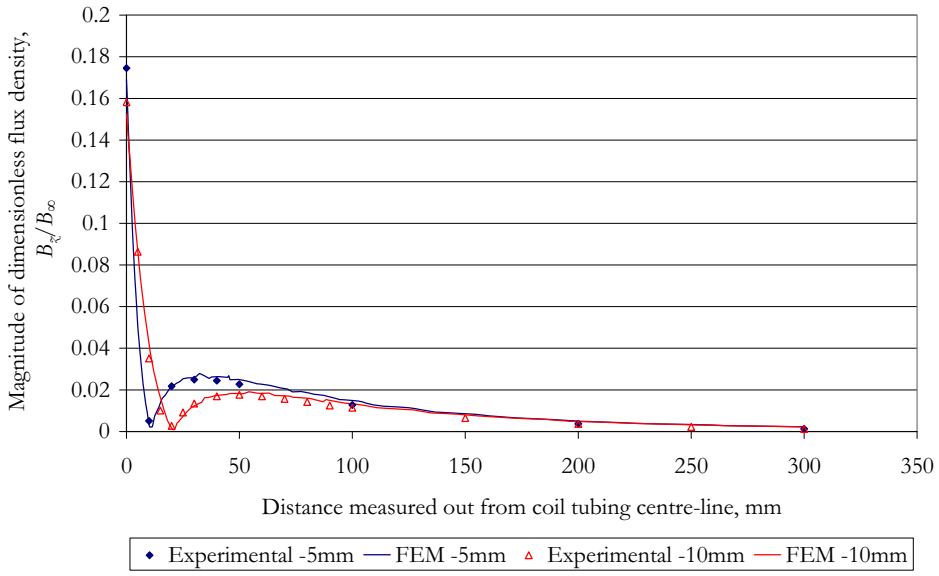

Figure 4.12-Comparison of the dimensionless flux density ($B_z/B\infty$) with radial position [mm] measured outwards from the current sheet diameter (D_{cs}) for coil #1. Note that 'absolute values' have been taken from the FEM model, as the Hall Effect probe does not report direction, only magnitude for AC fields. Direction of the field reverses at 15-20 mm out from the coil, i.e after reaching the x-axis.

As mentioned in *Section 2.2* (and in *Supplement 2* Figure 5), the heating rate should be impacted by the magnitude of the local z-component of the flux density, i.e. the phi-current on the surface of the work piece should be in proportion to the local and not the average flux density (ignoring the possible contribution due to the variation of the r-component of the magnetic field intensity in the z-direction). The heating rate should then vary proportionally to the square of the local z-component flux density.

In Figure 4.13 the square of the measured flux density using the axial Hall Effect probe is used for the X-axis (noting the average 3 mm offset due to the probe's 6 mm diameter), and is compared to the equivalent surface heating rate predicted by the 2D axial symmetric FEM model, which is plotted on the Y-axis. A regression line has been plotted and forced through the actual intercept, i.e. zero. It is concluded that with an $R^2 = 0.98$ this agreement tends to support the precision of both the numerical model and of the experimental techniques presented here.

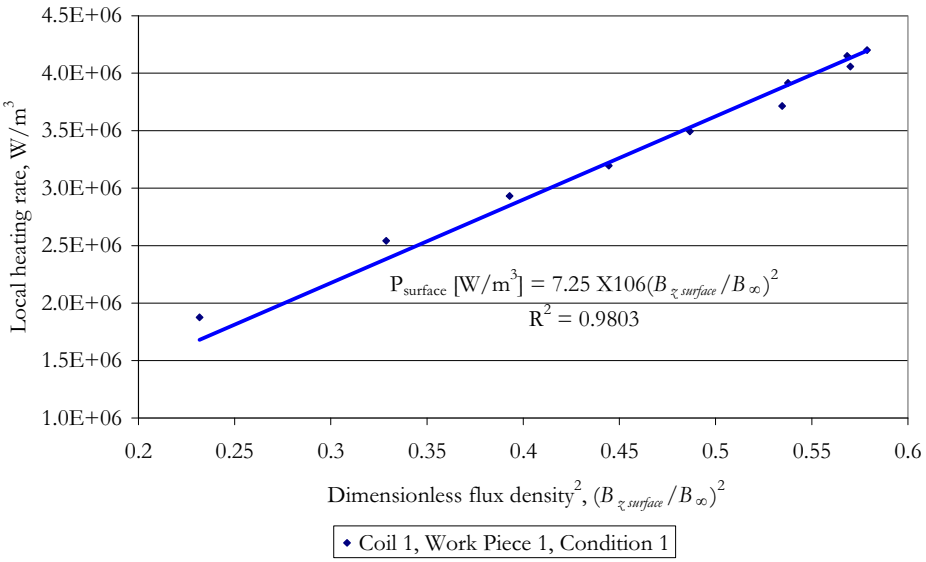

Figure 4.13-Comparison of 2D axial symmetric FEM modelling results of the local surface heating rate for 'short' coil #1 and work piece #1, at condition #1, with the square of the dimensionless measured local magnetic flux density $(B_{z\ surface}/B_{\infty})^2$.

Chapter 5

CONCLUSIONS AND FUTURE WORK

5.1 Conclusions

This investigation has shown that the magnetic field produced by a 'short' induction coil is much lower in magnitude than one would expect from the use of a long coil formula such as Equation (2). An improved 'short coil' correction factor, Equation (52), has therefore been proposed and experimentally validated at 50 Hz for application to induction heating of billets. Excellent agreement was achieved between experimental data and the analytical model estimates at 50 Hz for:

- the z-component of the magnetic flux density at the surface of the work piece [T] (typically ±2-3%),
- heating power [W] (typically ± 5%), and
- total coil and work piece reactive power [VAr] (<±1% error).

Analytical and FEM model work piece real power estimates were in consistent agreement at frequencies from 50 Hz to 500 kHz with differences of less than 5% for the short coil and 2% for the long coil over the entire range of frequencies. A similar level of agreement was also obtained for the work piece reactive power estimates.

Using the improved correction factor, the errors obtained in the estimates of work piece power have been reduced from approximately 15%, to an average value of <5%. Using Equation (52) also reduces the magnitude of the errors in power estimation from a factor of 2 in comparison with making a long coil assumption, i.e. assuming $k_N^* = 1.0$ for a 'short' coil.

The improved 'short coil' correction factor can be used to estimate the average flux density of a 'short coil' containing a work piece, with an error of <2-3%, based on the square root of the error in the work piece power estimation. Based on the better than

1% agreement of the reactive power estimates, the actual errors are expected to be smaller.

The improved accuracy of Equation (52) should allow for more accurate design of axially symmetric heating systems (e.g. billets and cylindrical furnaces) in the absence of FEM simulations. If combined with simulations, the analytical solutions are accurate enough to pre-define the modelling area of interest, e.g. determine nearly the exact optimal frequency and current for a given target power, coil and work piece combination.

Equation (52) can also be used to determine if a numerical model has been meshed correctly, if the magnetic domain size is sufficiently large and so on. While it is clear that with a validated numerical model that higher accuracy can be obtained, it is also possible to have highly inaccurate results due to modelling errors. Comparison with a 'hand calculated' value, limits the maximum possible error, even in the absence of empirical data.

For furnace and heating installation operators, Equation (52) allows for estimation of their power input, based on simple measurements that can be made in the 'field' (i.e. current, frequency and physical dimensions). This should allow for more precise operation of existing equipment.

The frequency corrected 'short coil' correction factor has also been found necessary to achieve accurate analytical solutions of the Lorentz forces produced by short coils [60] in electromagnetic stirring applications, which would otherwise contain approximately a factor of 2 error, depending on the coil shape factor.

A new equation for estimating the temperature coefficient of resistivity for aluminium alloys has been obtained and found to give excellent agreement in the FEM models used during this work.

Comparison of the 2 D axial symmetric FEM models with the measured local z-component flux density, has shown the expected quadratic relationship with local power density [W/m^3].

5.2 Future Work

Future work should focus on the correction of the bias found for Equation (52) and on derivation of a 2D factor, which would allow accurate estimation of local magnetic flux densities and the resulting longitudinal variation of the heating rate of the work pieces.

Additional experimental work at high frequency, with square or rectangular sectioned coils, would be of assistance in determining the true variation of the 'effective coil diameter' with frequency.

It has been experimentally verified that the external magnetic field is 'non-zero' and hence the reluctance of the external magnetic field will play a significant role in determining the overall magnetic flux density in a 'short' coil.

The installation of a split collar top and bottom, and laminated iron return path, should reduce the reluctance of the external return path and significantly increase the internal magnetic field strength (i.e. tend to increase the short coil correction factor, k^*_N towards a value of 1.0), while 'shielding' those working near the coil from exposure to any possible effects caused by exposure to strong magnetic fields.

The use of removable sections of the external flux path, to produce variable area 'air gaps' in the external magnetic circuit, can then be used to provide a means of fine control of the magnitude of the internal magnetic field inside of the coil and hence the rate of heating of the work piece for a fixed coil current.

REFERENCES

1. O. Heaviside, *Electrical Papers,* Vol. 1, (London: Macmillan & Co., 1892), 353-416.
2. J. Grzella, P. Sturm, J. Krüger, M. A. Reuter, C. Kögler, and T. Probst, "Metallurgical Furnaces," *Ullmann's Encyclopedia of Industrial Chemistry,* 22, (Weinheim: Wiley-VCH, 2012), 693-733.
3. S. de Ferranti, "Pioneer of Electric Power Transmission: An Account of Some of the Early Work of Sebastian Ziani de Ferranti, D. Sc., FRS (1864-1930)," *Notes and Records of the Royal Society of London,* 19, (1964), 33-41.
4. J. Härdén, "Recent Developments of the Kjellin and Röchling-Rodenhauser Electric Induction Furnaces," *Transactions of the Faraday Society,* 4, (1908), 120-125.
5. C. Elwell, "The Refining of Iron and Steel in Induction Type Furnaces," *Transactions of the American Institute of Electrical Engineers,* 30, (1911), 857-866.
6. T. Robertson, "Electric Steel-Making Furnaces," *Journal of the Institution of Electrical Engineers,* 53, (1915), 533-539.
7. E.F. Northrup, "Production of High Temperature and Its Measurement," *Transactions of the Faraday Society,* 13, (1918), 212-221.
8. E.F. Northrup, "Focus Inductor Furnace," US patent 1,378,187, (1921).
9. E.F. Northrup,, "Ladle Heating by High Frequency Currents," US patent 1,378,188, (1921).
10. E.F. Northrup, "Method and Apparatus for Electric Heating by High Frequency Currents," US patent 1,286,394, (1918).
11. E.F. Northrup, "High-Frequency Induction Furnace," US patent 1,694,792, (1928).
12. H. Nagaoka, "The Inductance Coefficients of Solenoids," *Journal of the College of Science,* 27, (1909), 18-33.
13. C. Burch and N. Davis, *An Introduction to the Theory of Eddy-Current Heating*, (London: E. Benn Limited, 1928).
14. N. Stansel, "Induction Heating - Selection of Frequency," *Transactions of the American Institute of Electrical Engineers,* 63, (1944), 755-759.
15. J. Vaughan and J. Williamson, "Design of Induction-Heating Coils for Cylindrical Nonmagnetic Loads," *Transactions of the American Institute of Electrical Engineers,* 64, (1945), 587-592.
16. C. Tudbury, *Basics of Induction Heating*, Vol. 1. (New York: John F. Rider, 1960).
17. R. Baker, "Design and Calculation of Induction Heating Coils'," *AIEE Transactions,* 57, (1957), 31-40.
18. J. D. Lavers, "Current, Force and Velocity Distributions in the Coreless Induction Furnace," PhD. Thesis, University of Toronto, (1970).
19. A. M. Ampère, *Mémoires sur L'électromagnétisme et L'électrodynamique* (Paris: Gauthier-Villars, 1921).
20. J. B. Biot and F. Savart, "Note sur le Magnetisme de la Pile de Volta," *Ann. Chim. Phys,* 15, (1820), 222-223.
21. M. W. Kennedy, S. Akhtar, J. A. Bakken, and R. E. Aune, "Review of Classical Design Methods as Applied to Aluminum Billet Heating with Induction Coils," *EPD Congress*, San Diego, California, February 27 - March 3, (2011), 707-722.
22. L. Lorenz, "Ueber die Fortpflanzung der Electricität," *Annalen der Physik,* 243, (1879), 161-193.

23. R. S. Weaver., (accessed on-line May 19, 2013), http://electronbunker.ca/CalcMethods.html. R. Weaver. [Online].
24. R. S. Weaver, "Practical Considerations in the Calculation of Kelvin Bessel Functions and Complete Elliptic Integrals K and E," October 26, (2009), 1-11.
25. R. Weaver., (accessed on-line May 19, 2013), http://electronbunker.ca/DL/NumericalExamples01.ods.
26. H. Wheeler, "Simple Inductance Formulas for Radio Coils," *Proceedings of the IRE,* 16, (1928), 1398-1400.
27. D. Knight. (accessed online, May 19, 2013), www.g3ynh.info/zdocs/magnetics/part_1.html.
28. *Copper Wire Tables Circular No. 31*, US Bureau of Standards, (1913).
29. E. B. Rosa and F. Grover, "Formulas and Tables for the Calculation of Mutual and Self Induction," *Scientific Papers of the Bureau of Standards,* No. 169., (1916), 5-231.
30. M. W. Kennedy, S. Akhtar, J. A. Bakken, and R. E. Aune, "Electromagnetically Enhanced Filtration of Aluminum Melts," *Light Metals*, San Diego, California, February 27 - March 3, (2011), 763-768.
31. J. S. Ames, *The Discovery of Induced Electric Currents,* Vol. 2, (New York: American Book Company, 1900).
32. E. J. Davies, *Conduction and Induction Heating*, (London: Peter Peregrinus on behalf of the Institution of Electrical Engineers, 1990).
33. H. Dwight and M. Bagai, "Calculations for Coreless Induction Furnaces," *Transactions of the American Institute of Electrical Engineers,* 54, (1935), 312-315.
34. J. A. Bakken, "Induksjonsovner - Teori og Virkemåte," Metallurgisk Institutt, NTH, 1993.
35. N. McLachlan, *Bessel Functions for Engineers*, (Gloucestershire: Clarendon Press, 1955).
36. P. Desai, H. James, and C. Ho, "Electrical Resistivity of Aluminum and Manganese," *Journal of Physical and Chemical Reference Data,* 13, (1984), 1131-1172.
37. R. Brandt and G. Neuer, "Electrical Resistivity and Thermal Conductivity of Pure Aluminum and Aluminum Alloys up to and Above the Melting Temperature," *International Journal of Thermophysics,* 28, (2007), 1429-1446.
38. S. Bakhtiyarov, R. Overfelt, and S. Teodorescu, "Electrical and Thermal Conductivity of A319 and A356 Aluminum Alloys," *Journal of Materials Science,* 36, (2001), 4643-4648.
39. T. C. Totemeier and C. J. Smithells, *Smithells Metals Reference Book*, (Oxford: Butterworth-Heinemann, 2004).
40. A. Roine, "HSC Chemisty Version 4.1," Outokumpu Oy, Finland, (1999).
41. Thermal Ceramics Company Pamplet, "Superwool® Plus Blanket Datasheet Code EU: 11-5-01 US: 11-14-401," www.thermalceramics.com.
42. M. W. Kennedy, S. Akhtar, J. A. Bakken, and R. E. Aune, "Analytical and Experimental Validation of Electromagnetic Simulations Using COMSOL®, re Inductance, Induction Heating and Magnetic Fields," presented at the COMSOL Users Conference, Stuttgart Germany, October 26-28, (2011), 1-9.
43. G. Howe, "The Application of Telephone Transmission Formulae to Skin-Effect Problems," *Journal of the Institution of Electrical Engineers,* 54, (1916), 473-480.
44. G. Howe, "The High-Frequency Resistance of Wires and Coils," *Journal of the Institution of Electrical Engineers,* 58, (1920), 152-162.
45. A. E. Kennelly, F. A. Laws, and P. H. Pierce, "Experimental Researches on Skin Effect in Conductors," *Transactions of the American Institute of Electrical Engineers,* 34, (1915), 1953-2021.
46. A. Kennelly and H. Affel, "Skin-Effect Resistance Measurements of Conductors," *Proceedings of the Institute of Radio Engineers,* 4, (1916), 523-574.
47. C.N. Hickman, "Alternating-Current Resistance and Inductance of Single Layer Coils," No. 472, *Scientific Papers of the US Bureau of Standards*, (1923), 73-104.
48. H. B. Dwight, "Skin Effect in Tubular and Flat Conductors," *Transactions of the American Institute of Electrical Engineers,* 37, (1918), 1379-1403.

49. H. B. Dwight, "Skin Effect and Proximity Effect in Tubular Conductors," *Transactions of the American Institute of Electrical Engineers,* 41, (1922), 189-198.
50. S. Butterworth, "Eddy-Current Losses in Cylindrical Conductors, with Special Applications to the Alternating Current Resistances of Short Coils," *Philosophical Transactions of the Royal Society of London. Series A, Containing Papers of a Mathematical or Physical Character,* 222, (1922), 57-100.
51. S. Butterworth, "Note on the Alternating Current Resistance of Single Layer Coils," *Physical Review,* 23, (1924), 752-755.
52. S. Butterworth, "On the Alternating Current Resistance of Solenoidal Coils," *Proceedings of the Royal Society of London. Series A,* 107, (1925), 693-715.
53. R. Medhurst, "High Frequency Resistance and Self-Capacitance of Single-Layer Solenoids," *Wireless Engineer*, February, (1947), 35-43.
54. R. Medhurst, "High Frequency Resistance and Self-Capacitance of Single-Layer Solenoids," *Wireless Engineer,* March, (1947), 80-92.
55. R. Medhurst and H. Resistance, "Q of Solenoid Coils," *Wireless Engineer*, September, (1947), 281.
56. W. Witzig, "Data on the High-Frequency Resistance of Coils," *Transactions of the American Institute of Electrical Engineers,* 66, (1947), 764-769.
57. P. Dowell, "Effects of Eddy Currents in Transformer Windings," *Proceedings of the IEE*, Vol. 113, No. 8, (1966), 1387-1394.
58. E. Fraga, C. Prados, and D. Chen, "Practical Model and Calculation of AC Resistance of Long Solenoids," *IEEE Transactions on Magnetics,* 34, (1998), 205-212.
59. A. Reatti and M. Kazimierczuk, "Comparison of Various Methods for Calculating the AC Resistance of Inductors," *IEEE Transactions on Magnetics,* 38, (2002), 1512-1518.
60. M. W. Kennedy, S. Akhtar, J. A. Bakken, and R. E. Aune, "Electromagnetically Modified Filtration of Aluminum Melts Part I: Electromagnetic Theory and 30 PPI Ceramic Foam Filter Experimental Results," Metallurgical and Materials Transactions B, DOI 10.1007%2Fs11663-013-9798-8, [Online] February 2013.